Geometry and Orientation Effects in Non-Uniformly Heated Microchannel Heat Exchangers Using Supercritical Carbon Dioxide

Saad A. Jajja[a], Jessa M. Sequeira[a], Brian M. Fronk[a,*]

[a]*School of Mechanical, Industrial and Manufacturing Engineering*
Oregon State University
Corvallis, OR 97331 USA

Abstract

There is growing interest to use supercritical carbon dioxide (sCO_2) as a working fluid in thermal management applications. This study investigates the thermal-hydraulic performance of microchannel heat sinks as a function of flow channel geometry and orientation at operating conditions representative of electronics cooling applications. Three different experimental test sections, subject to non-uniform heat flux boundary conditions, were investigated. Two of the test sections contained parallel arrays of rectangular microchannels with a hydraulic diameter of 750 μm and aspect ratios of 1 and 2, respectively. The third test section had a staggered array of diamond shaped micro-pins with a hydraulic diameter, based on the minimum flow area, of 525.2 μm. Data were collected for varying inlet temperature ($16 \leq T_{in} \leq 50$ °C), mass flux ($315 \leq G \leq 1000$ kg m^{-2} s^{-1}), and heat flux ($20 \leq q'' \leq 40$ W cm^{-2}) at a fixed reduced pressure (P_R) of 1.1. A data analysis method using 2-D and 3-D heat transfer models of the test sections was used to calculate the average heat transfer coefficients for each experimental condition. Additionally, a pressure drop model was developed to resolve the total measured pressure drop into its components. The results of this study indicate that the turbulent convective heat transfer was independent of orientation (top versus bottom heating) for square microchannel (aspect ratio = 1) for the conditions investigated. Increasing the aspect ratio from 1 to 2 led to an enhancement in thermal transport. Finally, the heat transfer performance of the staggered pin array flow geometry was superior to the rectangular channels, but this enhancement in heat transfer was commensurate with the increase in pressure drop. Based on these results, this paper

concludes with general design recommendations for those considering the early adoption of supercritical carbon dioxide for thermal management applications.

Keywords: Thermal Management, Supercritical, Carbon Dioxide, Microchannel, Aspect ratio, Micro-pin Array, Turbulent Flow, Non-Uniform Heating, Electronics Cooling

1. Introduction and Prior Work

Supercritical carbon dioxide (sCO_2) has garnered wide interest as a working fluid in power cycles and heat pump systems. Its superior thermophysical properties near the critical point also make it a potentially attractive working fluid for the thermal management of high heat fluxes ($\geq$ 100 W cm^{-2}) in microchannel geometries [1, 2]. For operation in the turbulent flow regime, thermal transport from the heated wall to the bulk of the fluid is limited by the diffusion dominated region of the boundary layer. This is shown schematically in Figure 1. The thickness and hence the resistance associated with this region shows an inverse dependence on the molecular Prandtl number [3, 4]. Supercritical carbon dioxide exhibits a large increase in its heat capacity and Prandtl number in the proximity of its pseudo-critical point, as shown in Figure 2, thereby enhancing thermal transport and motivating the use of (sCO_2)for the efficient management of high heat fluxes.

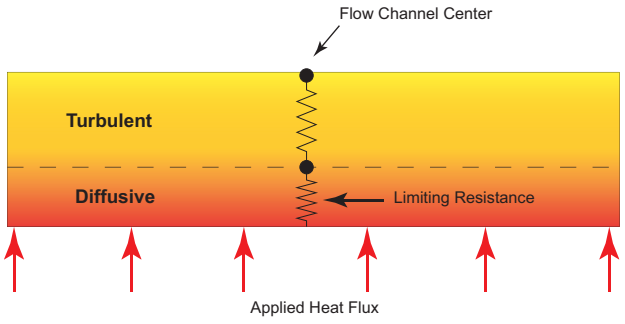

Figure 1: Schematic of a fully developed thermal turbulent boundary layer for heated internal flow.

*Corresponding author
Email address: brian.fronk@oregonstate.edu (Brian M. Fronk)

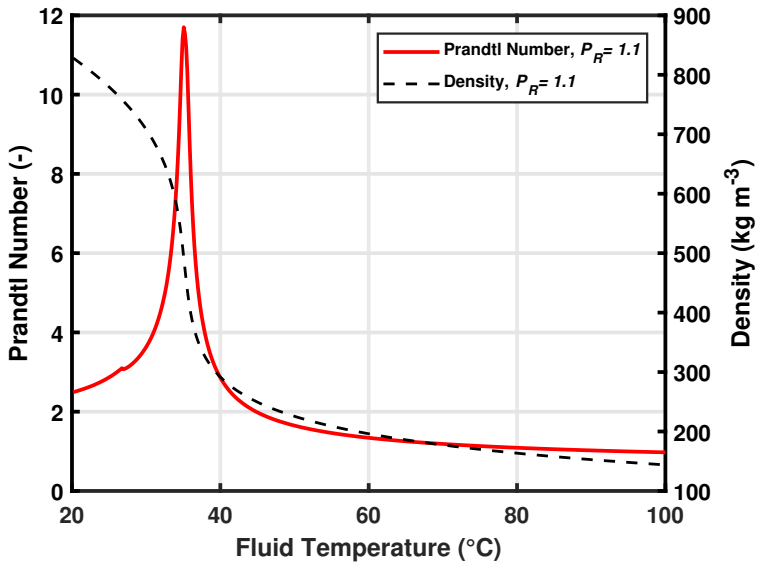

Figure 2: Prandtl number and density variations of carbon dioxide as a function of temperature for a reduced pressure of 1.1.

However, as shown in Figure 2, sCO_2 also exhibits a steep gradient in its density in the proximity of its pseudo-critical point. Steep axial and transverse density variations will alter the turbulent transport in a manner which can either complement or suppress the enhancement due to a higher Prandtl number. Transverse and axial variations in the fluid density will induce buoyancy forces and flow acceleration effects, respectively.

The consequence of the bulk axial acceleration of the fluid is to reduce the turbulent thermal transport [5, 6]. This is due to the favorable pressure gradient acting as a stabilizing influence and suppressing the ejection of stream wise velocity fluctuations away from the near wall region [3, 6, 4, 7]. If flow acceleration conditions persist for a significant length of the test section, as determined by some criterion, e.g. [8], the turbulent boundary layer can undergo a reverse transition to a laminar boundary layer, yielding a sharp reduction in the thermal transport capabilities. Flow acceleration effects are orientation independent, unlike buoyancy's influence on turbulent heat transfer.

For turbulent flows in buoyancy-aided vertical flow configurations, buoyancy acts to suppress streamwise and cross stream velocity fluctuations [7, 9], thereby leading to a reduction in turbulent thermal transport. However, after an initial reduction in thermal transport,

turbulence production is restored in the boundary layer which leads to a recovery in the heat transfer. This recovery can be explained either based on shear-stress/velocity profile shape arguments [10, 11] or can be interpreted as flow transitioning to a turbulent natural convection boundary layer. The evidence for this comes from the fact that the location for the maximum in stream wise velocity fluctuations is offset from the location of the maximum in the mean velocity [9]. This is a characteristic of a turbulent natural convection boundary layer as outlined in these experimental investigations [12, 13]. A recent experimental investigation by Theologou *et al.* [14] explored the applicability of some of these criteria for nuclear power applications. They showed that criteria developed by Jackson [10] were able to predict the deteriorated heat transfer for vertical flow configurations.

For buoyancy-opposed flow configurations, there is an enhancement in cross stream and stream wise velocity fluctuations and a reduction in the thickness of the viscous-sublayer region [7, 9]. This leads to an enhancement in thermal transport, relative to pure forced convective heat transfer, from the heated wall to the bulk of the flow.

Buoyancy's influence on supercritical heat transfer in horizontally orientated test sections can be seen in the recent investigations of Pidaparti *et al.* [15] and Bazargan *et al.* [16]. Both studies reported circumferential variations in the tube wall temperatures, similar to the earlier observations reported by Adebiyi and Hall [17]. This circumferential tube wall temperature variation can be attributed to two separate effects as distinguished by Petukhov and Polyakov [18]. The structural effect of density fluctuations enhances turbulence production at the bottom wall and suppresses turbulence at the channel top wall. This degrades and enhances thermal transport at the tube top and bottom walls, respectively. The second effect, common to both laminar and turbulent flows, is associated with the bulk fluid motion being setup in the flow cross section by mean density gradients. This enhances thermal transport at the bottom wall and degrades it at the top wall [19].

While the role of buoyancy and flow acceleration for supercritical flows is accounted for in some mechanistic models developed for uniformly heated macroscale test sections [10, 20, 11, 21, 22, 18], it is unclear if the same insights extrapolate to the non-uniformly heated microscale geometries typically encountered in thermal management applications.

For instance, in horizontal flow channels, models accounting for buoyancy's influence on heat transfer with uniform heating account for both stable and unstable stratification conditions existing simultaneously in the flow cross section. This will not be the case when the applied heat flux is limited to a single wall of the flow channel. Additionally, using the channel hydraulic diameter as a length scale may not be appropriate to assess the magnitude of the buoyancy forces in horizontal flow configurations.

For turbulent boundary layers, the largest resistance and hence the steepest temperature gradient is limited to the near-wall conduction dominated region. Therefore for supercritical fluids, it is in this region that the biggest density gradient will be present. As observed in the recent numerical investigation of Nabil and Rattner [23], for conditions when the pseudo-critical temperature was reached within the boundary layer, plumes of fluid could be seen rising from the bottom walls of the microchannel simulated in their study. Based on conventional heat transfer theory, it can be argued that the conduction dominated region will only become unstable, giving rise to thermals/plumes, if the Rayleigh number is of the order 10^3. This Rayleigh number can either be evaluated by using the thickness of the conduction dominated region as a length scale or the channel hydraulic diameter. Using the channel hydraulic diameter as the length scale can possibly lead to an erroneous conclusion that the conduction region is unstable, leading to the formation of thermals/plumes. This false conclusion can be carried one step further by then saying that these plumes are altering the universal velocity and temperature profiles, causing the thermal transport to deviate from pure forced convective conditions.

In addition to varying thermophysical properties, buoyancy, and flow acceleration, the flow geometry can have a large impact on near-critical convective heat transfer. In our prior work, we experimentally investigated the heat transfer of sCO_2 in a parallel array of square (AR = 1) microchannels with non-uniform heat flux boundary conditions applied from the bottom [24]. We developed a 2-D and 3-D simulation approach to calculate the average convective heat transfer coefficient from measured data with low uncertainty ($<$ 10%), while accounting for conjugate heat transfer effects in the test section. Experiments were conducted for mass flux from 500 kg m^{-2} s^{-1} to 1000 kg m^{-2} s^{-1} , fluid inlet temperatures

from 16°C to 50°C , heat flux of 20 and 40 W cm^{-2}, and at reduced pressures of 1.03 and 1.1. In that study, the highest heat transfer coefficient reported was 13000 W m^{-2} K^{-1} for an applied heat flux of 20 W cm^{-2} and a mass flux of 1000 kg m^{-2} s^{-1}. The heat transfer coefficient decreased to 8600 W m^{-2} K^{-1} (decrease of 56 percent) for the same experimental conditions when the heat flux was doubled to 40 W cm^{-2}. This degradation suggests that alternative channel geometries, such as higher aspect ratio rectangular channels and micro-pin arrays must be investigated to provide cooling of even higher heat fluxes.

For rectangular geometries, channel aspect ratio is a critical parameter in subcritical single phase fluids for thermal management applications [25, 26, 27]. This is especially true for the laminar flow regime where the heat transfer coefficient has a strong dependence on the entire thickness of the thermal boundary layer, as shown in equation (1). For internal channel flows with a fixed hydraulic diameter, increasing the aspect ratio leads to higher heat transfer coefficients [28] due to the shorter diffusion length to the bulk. This has been experimentally observed for rectangular microchannel geometries using subcritical water, where an increase in channel aspect ratio enhanced the convective heat transfer in the laminar flow regime [29].

$$\alpha_{lam} \approx \frac{k}{\delta_t} \tag{1}$$

For turbulent flows, the largest temperature gradient in the thermal boundary layer is in the diffusion dominated viscous sub-layer region and therefore, the heat transfer coefficient for turbulent channel flows depends upon the sub-layer thickness as shown in equation (2). If the thickness of the sub-layer is significantly smaller than the channel hydraulic radius, turbulent thermal transport is expected to be independent of the channel shape [30].

$$\alpha_{turb} \approx \frac{k}{\delta_{cl}} \tag{2}$$

However, Li and Olsen [31], using Micro-PIV, explored the effects of channel aspect ratio on turbulent flow in rectangular microchannels for adiabatic boundary conditions. Their study concluded that an increase in the channel aspect ratio caused an increase in the near wall Reynolds shear stress. A similar observation was reported by Jones [32]. The Reynolds analogy then suggests that an increase in near-wall shear stress will lead to more effective

thermal transport for heating boundary conditions. This has been experimentally observed for single-phase, subcritical flows with constant properties, where microchannel width and height ratios influenced the turbulent thermal transport [29]. There is limited information on the effect of aspect ratio for the varying property and turbulent regime conditions of interest in this study for near-critical flows.

Micro-pin arrays are another method to enhance heat transfer in single-phase, subcritical heat sink applications. In Jajja *et al.* [33], we reported preliminary results of supercritical heat transfer in diamond shaped micro-pins for turbulent flow. This was motivated by the fact that most of the prior work and correlations available in the literature on micro-pin geometries have focused on laminar flow. For instance, in the laminar flow flow regime, micro-pin fin based heat sinks have been used to manage applied heat fluxes ranging from 3.8 W cm^{-2} to 790 W cm^{-2} [34, 35]. Additionally, most studies involving micro-pin heat sinks in the laminar flow regime were concerned with the predictive capability of correlations developed for macroscale pin fin geometries. A systematic study conducted by Prasher *et al.* [36] evaluated the pressure drop and thermal resistance for micro-pin fin based geometries in the laminar flow regimes. They considered circular and square pins with dimensions ranging from 50 μm to 150 μm. It was concluded that existing correlations, developed for macro-pin fin geometries, failed to predict the thermal-hydraulic performance of micro-pin fin geometries. Similar conclusions were reported by [37, 38] for micro-pin based heat sinks with single phase, subcritical working fluids.

For turbulent flow regime, some correlations exist for macroscale staggered geometries, e.g. [39, 40]. However, these correlations are only applicable for a specific range of geometric parameters, e.g. transverse pitch or pin height to diameter ratio. Recently, a correlation was proposed by Rasouli *et al.* [41] for single phase heat transfer in staggered diamond shaped micro-pin fins. The dimensions of the test section used in the investigation of Rasouli *et al.* closely matches our own. However, the correlation was developed for Reynolds number, based on pin fin hydraulic diameter, ranging from 8 to 1189. For these Reynolds numbers, the fluid is not expected to be in the turbulent flow regime upon entering the heat sink. Additionally, none of the available correlations for turbulent flows in either macroscale or

microscale pin array geometries were developed considering the effects of rapidly varying thermophysical properties. Such conditions will be encountered in heat exchangers that employ sCO_2 as a working fluid and operate in the proximity of the pseudo-critical point.

Given the limited investigation of near-critical heat transfer in microchannels and micro-pins at conditions relevant to electronic cooling, the present study is focused on quantifying and comparing the heat transfer and pressure drop performance of sCO_2 for a variety of channel flow geometries. This study also empirically and analytically evaluates the significance of buoyancy forces on heat transfer in non-uniformly heated heat exchangers and the appropriateness of criterion developed for uniformly heated flows that were not considered in our prior study [24].

Three different heat exchanger geometries, operating in a horizontal orientation, are considered. Two of the test sections had parallel, rectangular microchannels with a hydraulic diameter of 750 μm and aspect ratio 1 and 2. The third had a staggered array of diamond shaped micro-pins with a hydraulic diameter of 679 μm (based on the minimum flow area). Data from [24] (square microchannels, bottom heated flow) and [33] (preliminary micro-pin data) were combined with new data for higher aspect ratio channels and different heating orientations to facilitate comparison of geometries, assessment of buoyancy (orientation) effects, and evaluation of heat transfer models. Heat transfer and pressure drop data included results for varying bulk inlet temperature ($16 \leq T_{in} \leq 50$ °C), mass flux ($300 \leq G \leq 1000$ kg m^{-2} s^{-1}), heat flux ($20 \leq q'' \leq 40$ W cm^{-2}) and reduced pressure (P_R) of 1.1. All experiments were conducted with horizontal flow. Experiments were conducted for bottom heated and top heated conditions using the square microchannel test section (aspect ratio = 1), and bottom heating only for the rectangular microchannel (aspect ratio = 2) and micro-pin array.

2. Experimental Approach and Data Analysis

A detailed description of the experimental loop and the heat transfer data analysis methodology was reported in [24], however, a summary is provided here for completeness.

2.1. Test Loop

The experimental loop used is comprised of four main components. A tube-in-tube pre-heater is used to control the inlet temperature of the sCO_2 as it enters the test section. Heated sCO_2 from the test section is cooled in a tube-in-tube post-cooler that is coupled to a 3 kW chiller. A gear pump is used to circulate the sCO_2 in the entire experimental loop. To control the pressure inside the loop, a 0.95 L accumulator, connected to a high pressure (17.5 MPa) Nitrogen tank is used. The schematic of the experimental facility is shown in Figure 3.

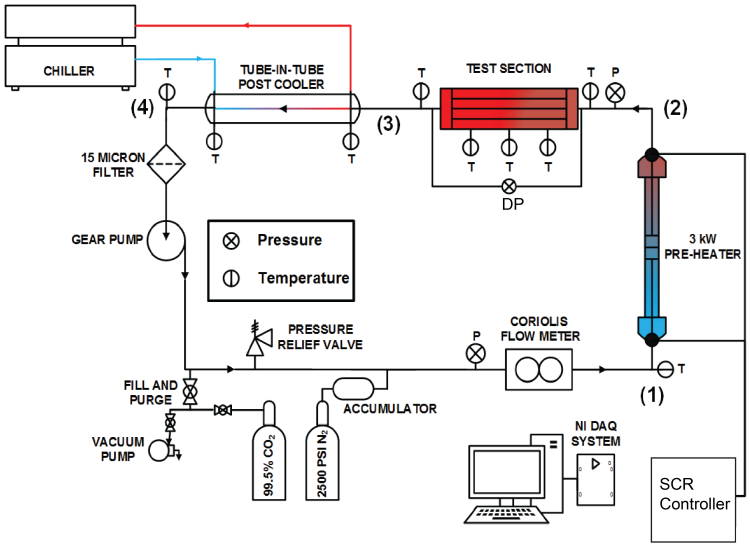

Figure 3: Schematic of the experimental facility.

Also shown in the schematic of the experimental facility are the locations of different instruments that are used to record bulk fluid temperatures, flow rate, and pressure. The bulk fluid temperatures of sCO_2 in the flow loop are measured by calibrated type - T thermocouples. The details and the locations of additional temperature measurements in the test section are presented in the subsequent sections. The absolute pressure and the differential pressure drop of sCO_2 across the test section is measured by Rosemount (Model 3051 SMV) pressure transducer. This transducer can measure absolute pressures ranging from 0 to 24.8 MPa and differential pressures in the range of 0 to 62.2 kPa. A Coriolis flow

meter, with a range of 0 to 325 kg hr^{-1}, is used to measure the mass flow rate of the sCO_2 in the test loop.

The current/voltage signals from these transducers are routed to a data acquisition system. This system consists of National Instrument cards that take either current or voltage signals as inputs (Model NI-9205, NI-9211, NI-9214 and NI-9203) and then send the output signal to a graphic user interface developed to display and record the raw experimental data.

2.2. Test Sections

Figure 4 shows a schematic of the test sections used. In each test section, the total flow length was 50 mm, with the first 30 mm designated as the development length. Heat flux was applied to the final 20 mm by a 100 W cartridge heater. The flux was calculated using data from six calibrated type - K thermocouples. Each test section was fabricated from 316/316L dual certified stainless steel with different internal flow geometries.

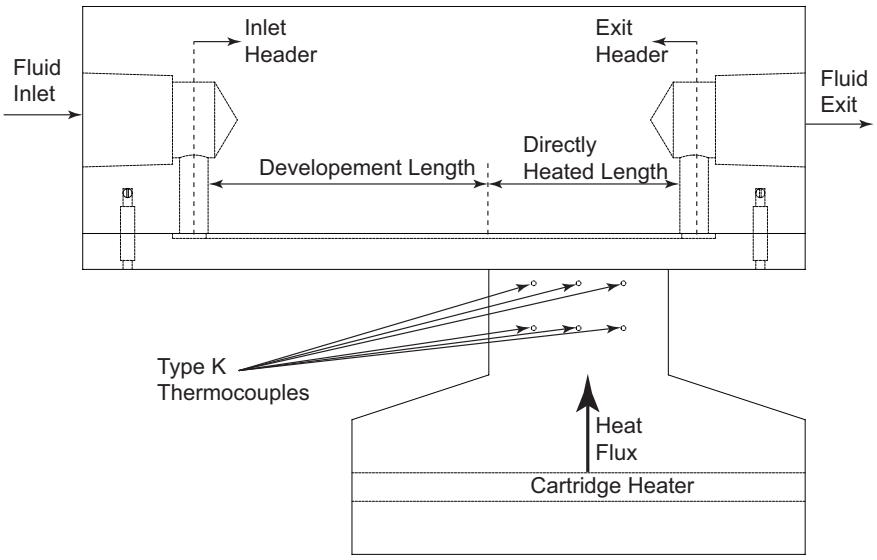

Figure 4: Schematic of the side view of the complete test section. This external design stayed consistent for all three test sections used in the current investigation.

Two of the test sections had microchannel based flow passages of varying aspect ratio (1 and 2), while the third had an array of staggered diamond shaped pins. Figure 5 shows the details of the internal geometry of the micro-pin array and the microchannel test sections.

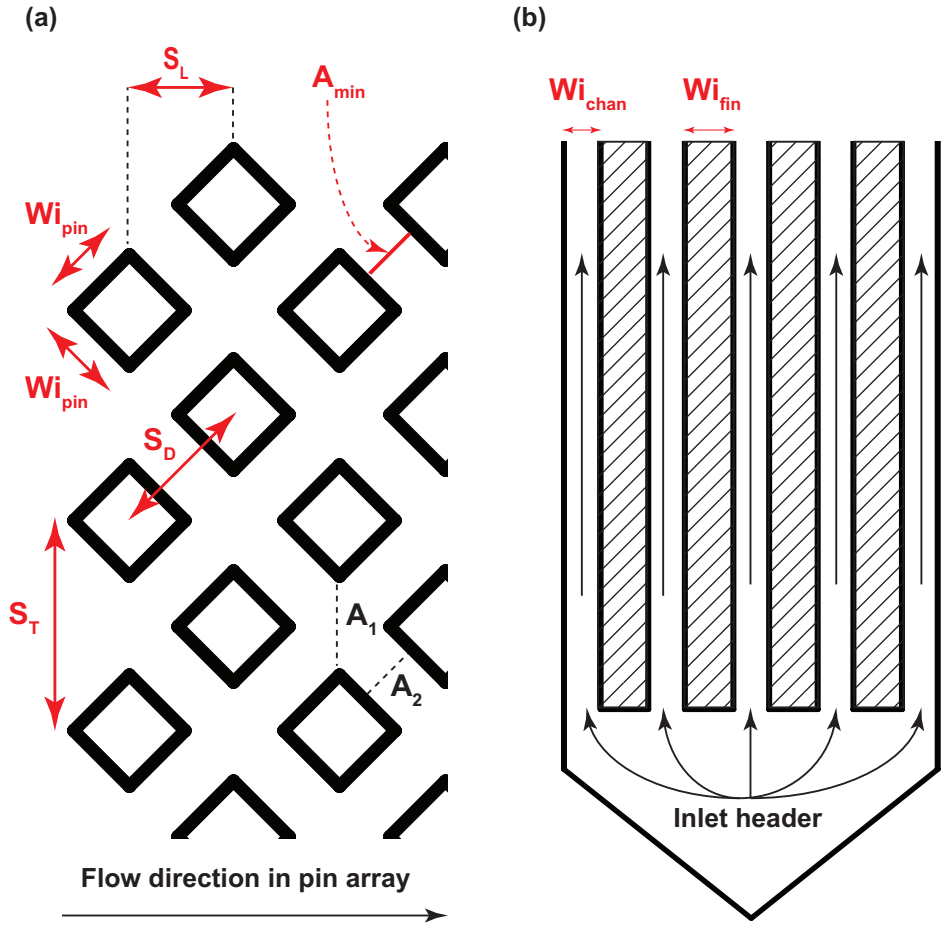

Figure 5: Details of the internal geometry of the test sections. (a) Staggered pin array with a pin height (H_{pin}) of 530.2 μm (into the page). The flow direction in the pin array is from left to right. (b) Microchannel test section with a channel length (L_{chan}) of 50 mm, measured from where the fluid leaves the inlet header and enters the exit header.

The dimensions associated with these internal features can be found in Tables 1 and 2, respectively.

For the staggered micro-pin array the minimum flow area (A_{min}) occurred at cross section labeled as "A_2" in Figure 5 (a). The hydraulic diameter associated with this flow area ($D_{A,min}$) is then evaluated as shown in equation (3). The mass flux through the pin array was defined by using the total minimum flow area in the pin array as shown in equations (4) and (5).

$$D_{A,min} = \frac{4(S_D - \sqrt{2}Wi_{pin})(H_{pin})}{2[H_{pin} + (S_D - \sqrt{2}Wi_{pin})]} \tag{3}$$

Table 1: Details of the internal geometry of the micro-pin array test section.

H_{pin}(μm)	Wi_{pin} (μm)	$D_h = \sqrt{2}$ W_{pin}(μm)	S_D(μm)	S_L (μm)	S_T (μm)	$D_{A,min}$(μm)	Wi_{Array} (mm)	No. of Pins (-)
530.2	633.4	895.8	1416	992	2000	525.15	10.62	225

Table 2: Details of the internal geometry of the microchannel based test sections.

Test Section	H_{chan}(μm)	Wi_{chan} (μm)	$D_h = \frac{4A_c}{Per_{wet}}$ (μm)	L_{chan}(mm)	AR = $\frac{Wi_{chan}}{H_{chan}}$	Wi_{fin} (μm)
Test Section "A"	737.3	750.0	743.6	50	1.01	991.8
Test Section "B"	566.9	1125.6	754.1	50	1.98	993.5

$$A_{min,tot} = \frac{Wi_{array}}{S_T}[H_{pin}2(S_D - \sqrt{2}Wi_{pin})] \tag{4}$$

$$G_{array} = \frac{\dot{m}_{tot,array}}{A_{min,tot}} \tag{5}$$

2.3. Heat Transfer and Pressure Drop Data Reduction

This section presents the methodology used to calculate the average heat transfer coefficients in the flow channels and the associated frictional pressure drop from measured parameters.

2.3.1. Heat Transfer Analysis

The details of the heat transfer modeling along with a sample calculation are presented in [24]. However, to ensure a smooth readability of the current paper, a brief summary of the modeling approach will be presented here.

In the current design of the experimental test section, shown in Figure 4, heat transfer to the directly heated length of the flow channels cannot be considered one-dimensional. Heat leakage from the directly heated region to the upstream development length and the test section top cover requires a three-dimensional heat transfer analysis to calculate the average heat transfer coefficient in the flow channels. A two-dimensional resistance network model of the bottom portion of the test section was integrated with a three-dimensional conjugate heat transfer analysis of the entire test section in COMSOL Multiphysics [42].

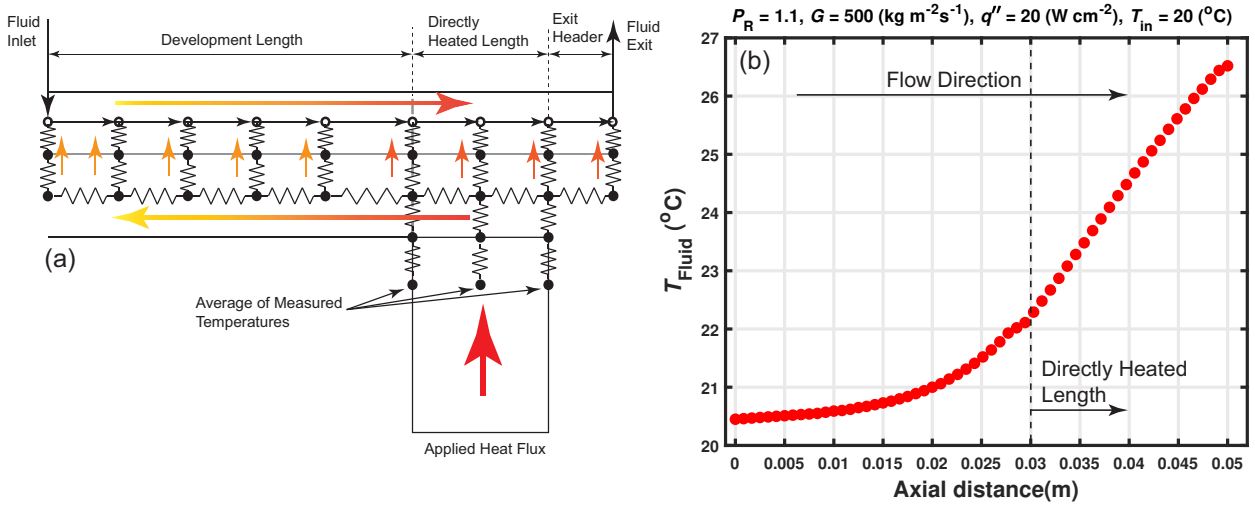

Figure 6: (a) Schematic of resistance network model and (b) fluid temperature profile calculated by the resistance network model for a microchannel test section with an aspect ratio of 1.

The two-dimensional resistance network model, shown in Figure 6(a), accounts for the axial conduction in the test section body and outputs the variation of the bulk fluid temperature along the flow channels as shown in Figure 6(b). Additionally, Figure 7 shows the calculated heat flux distribution along the bottom portion of the test section. While heat flux is highest in the "heated" region of the test section, the effects of axial conduction into the development length can also be seen. Failure to account of the 3D conjugate effects would lead to erroneous results. The resistance network model was developed using the Engineering Equation Solver (EES) platform [43] and the distribution of the heat flux as predicted by this model, have been compared against the predictions of the conjugate heat transfer analysis conducted in COMSOL Multiphysics. The reader should refer to the prior work of the authors for more details on this comparison [24].

The fluid temperature profile from the resistance network model is then used to specify a constant convective boundary condition in COMSOL, where the entire test section is being analyzed. The output of the three-dimensional analysis in COMSOL is the temperature distribution in the entire test section, allowing for a comparison of the numerically predicted temperatures at the flux meter thermocouple location to their experimentally measured values. For a particular set of experimental conditions, the value of the average heat transfer

coefficient in the flow channels is varied until the numerically predicted and experimentally measured temperatures at the flux meter location are within ± 0.22 °C of each other. The reader should consult [24] for reasons behind the choice of this particular tolerance and for more details regarding the modeling approach.

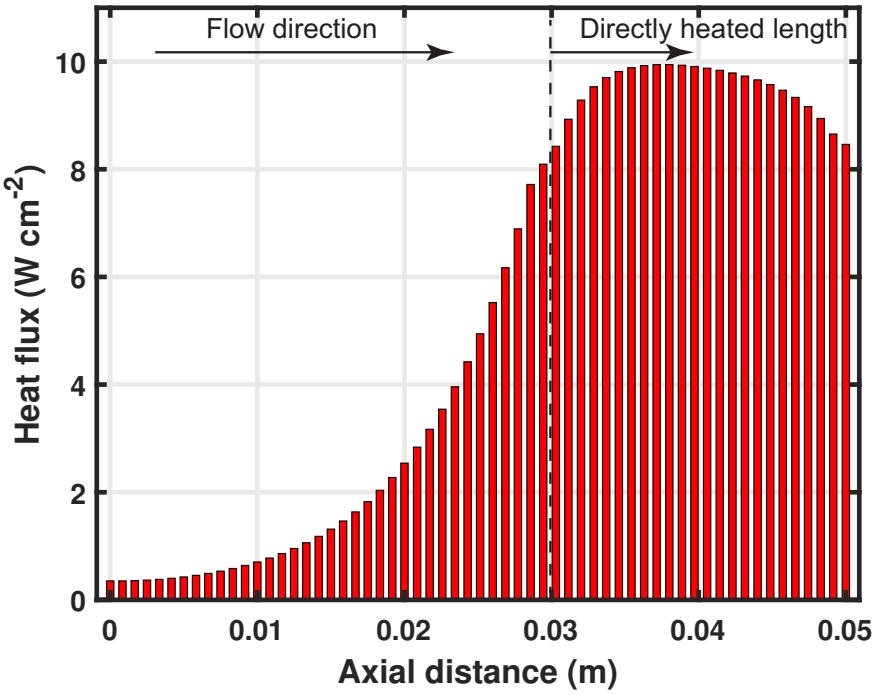

Figure 7: Calculated axial distribution of local heat flux from the bottom portion of the test section to the flow channels with an aspect ratio of 1. This heat flux distribution is representative of a test case with a reduced pressure of 1.1, applied heat flux of 20 W cm^{-2}, mass flux of 500 kg m^{-2} s^{-1} and an inlet temperature of 20°C.

2.3.2. Pressure Drop Analysis

The total pressure drop across the test section was measured by using a Rosemount 3051 SMV pressure transducer with a total experimental uncertainty of ± 0.12 kPa. This measured pressure drop is represented in equation (6) as the sum of its individual components.

$$\triangle_{P,meas} = \triangle_{P,fric} + \triangle_{P,acc} + \triangle_{P,minor} + \triangle_{P,cp} \tag{6}$$

To isolate the frictional pressure drop in the flow channels, the pressure drop associated with several minor losses in the test sections, acceleration of the bulk fluid, and connecting

tubing to the test section were calculated and subtracted from the total measured pressure drop across the test section. Figure 8 shows the locations of the various major and minor losses (labelled "A" through "H"). The type of minor losses encountered stay consistent throughout the three test sections tested.

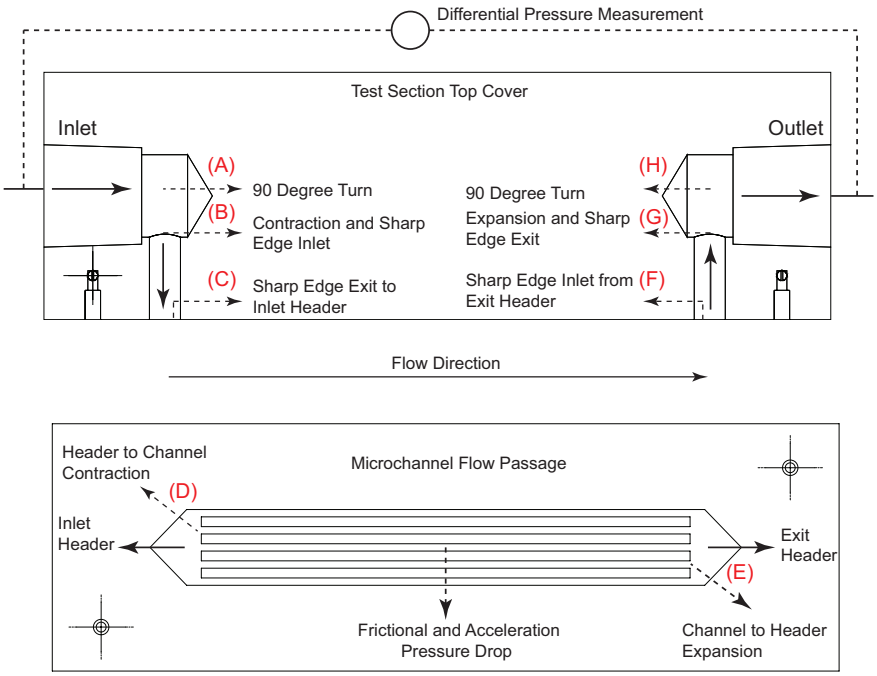

Figure 8: Fluid flow path and minor loss locations for pressure drop analysis in the microchannel test section. The minor losses in the test section top cover are consistent for all three test sections used in the current investigation.

Upon entering the test section, the fluid encounters a simultaneous 90^0 bend in the flow direction and a reduction in the diameter of the flow channel (location A in Figure 8). Additionally, upon entering the smaller diameter flow passage, there is a minor loss associated with a sharp edged pipe inlet and a sharp edged pipe exit when the fluid enters the inlet header (B and C). An additional minor loss occurs due to a reduction in the flow channel dimensions as the fluid enters the microchannels/micro-pin array from the inlet header (D). As the fluid leaves the microchannels/micro-pin array and enters the exit header, it experiences a loss associated with an expansion in the flow passage (E). Upon entering the test section top cover, the fluid encounters a loss associated with sharp edge

inlet, exit (F), channel expansion (G) and a 90^0 change in flow path (H). Pressure losses associated with each of these minor losses were calculated by determining the respective K values (resistance coefficients).

The loss due to the 90^0 change in the flow path was calculated using the minor loss coefficient (K value) for a miter bend as reported in [44] and shown in Equation (7). Here, f_{turb} is the friction factor for fully rough flow in a channel as represented by equation (8) and adopted from [45]. The absolute roughness throughout the test section was assumed to be 0.55 μm which was measured by ZeScope Optical Profiling System (Zemetrics, S/N: 08Z2015) in the test section flow channels [46]. The relative roughness was then calculated as the ratio of absolute roughness and the channel flow diameter.

$$K_{MB} = 60(f_{turb}) \tag{7}$$

$$\frac{1}{f_{turb}^{0.5}} = -2.0log\frac{\epsilon/D_{av}}{3.7} \tag{8}$$

The minor loss coefficients associated with sharp edged entrances and exits were assigned "K" values of 0.5 and 1, respectively [44]. Minor loss coefficients associated with a sudden contraction and expansion of the flow passage [44] were used to model the reduction/increase in the pipe diameter across the inlet/outlet bends and the entrance/exit from the microchannels/micro-pin array, as shown in Equations (9) and (10), respectively.

$$K_{SC} = 0.5\Big(1 - \frac{D_s^2}{D_l^2}\Big) \tag{9}$$

$$K_{SE} = \Big(1 - \frac{D_s^2}{D_l^2}\Big)^2 \tag{10}$$

For the minor losses associated with sharp inlets and exits, K values of 0.5 and 1.0 were used, as outlined in [44].

The calculated minor loss coefficients were assigned a conservative relative uncertainty of $\pm 50\%$ due to the simplifying assumptions made in the actual geometries of the bends, expansions and contractions. This approach is similar to that adopted by [47, 48].

Once all the minor loss coefficients were calculated, the total pressure loss associated with all the minor loss was calculated by equation (11), where the density was evaluated at the test section inlet absolute pressure and either the inlet or outlet temperature depending on minor loss location. For instance, the bulk velocity associated with the inlet header to channel contraction was evaluated by calculating the fluid density at the test section inlet absolute pressure and temperature.

$$\triangle_{P,minor} = \sum_{i=1}^{n} K_i \frac{V_i^2}{2} \rho_i \tag{11}$$

The pressure loss associated with the acceleration of the bulk fluid was evaluated from the momentum balance shown in equation (12).

$$\triangle_{P,acc} = (\rho_{out} V_{out}^2 - \rho_{in} V_{in}^2) \tag{12}$$

The pressure loss associated with the 50 mm connecting tubing on either side of the test section was calculated by using the Churchill [49] Darcy friction factor correlation for turbulent flow, shown in in equations (13) through (15).

$$f_{turb} = 8\Big[\Big(\frac{8}{Re_{D_h}}\Big)^{12} + (\theta_1 + \theta_2)^{-1.5}\Big]^{\frac{1}{12}} \tag{13}$$

$$\theta_1 = \Big[2.457 ln\Big[\Big(\frac{7}{Re_{D_h}}\Big) + 0.27\Big(\frac{\epsilon}{D_h}\Big)\Big]^{-1}\Big]^{16} \tag{14}$$

$$\theta_2 = \Big[\frac{37530}{Re_{D_h}}\Big]^{16} \tag{15}$$

2.3.3. Validation of Pressure Drop Modeling

Adiabatic pressure drop experiments in the square channel (aspect ratio = 1) test section were conducted to validate the pressure drop modeling approach. The experimentally determined frictional pressure drop, as described in the preceding subsection, was compared against the predictions of Darcy friction factor correlations for turbulent flow. The Churchill friction factor correlation for turbulent flow [49], shown in equations (13) through (15), was used to predict turbulent pressure drop. Turbulent friction factor can be considered independent of the channel shape [30] and therefore for the rectangular microchannel with an aspect ratio of 1, correlations developed for rough circular tubes should be applicable.

The Reynolds number for the calculation of these friction factors was evaluated by determining the viscosity of the supercritical carbon dioxide at the test section inlet absolute pressure and the bulk fluid temperature. Theoretically predicted pressure drops associated with these friction factors were evaluated by using equation (16). The channel velocity and the density was evaluated at the bulk fluid temperature.

$$\triangle_{P,turb} = f_{turb} \frac{L_{chan}}{D_h} \frac{V_{chan}^2}{2} \rho_{chan} \tag{16}$$

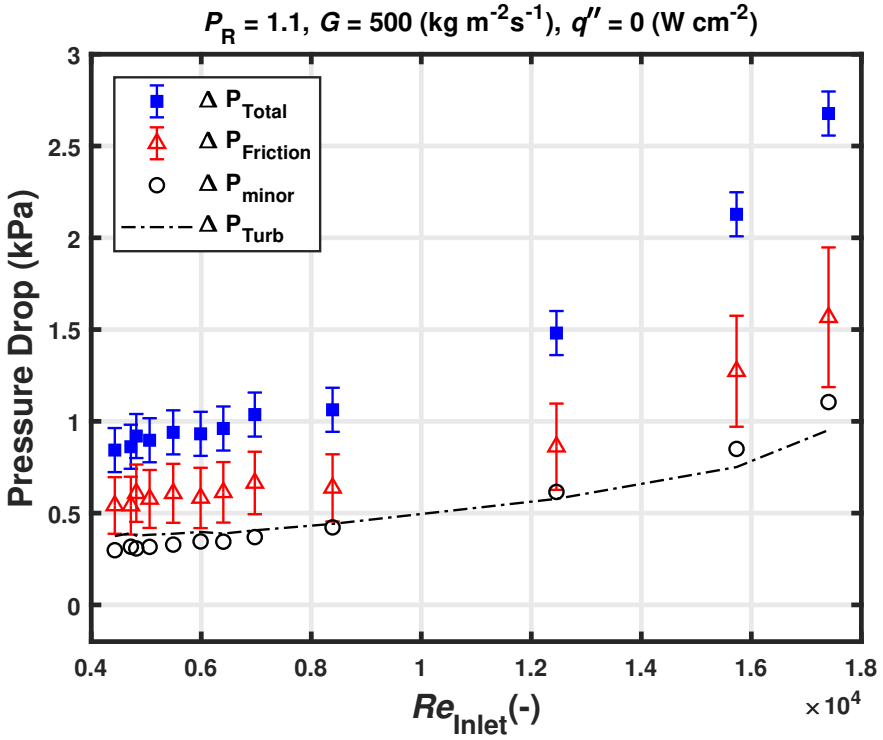

Figure 9: Pressure drop versus inlet Reynolds number for $P_R = 1.1$, $G = 500$ kg m^{-2} s^{-1}, $q^{''} = 0$ W cm^{-2} in microchannel based test section with an aspect ratio of 1.

Representative results for the adiabatic (heat flux of 0 W cm^{-2}) test case with a mass flux of 500 kg m^{-2} s^{-1} and reduced pressure of 1.1 are shown in Figure 9. This Figure shows the total measured pressure drop (with uncertainty), the calculated frictional pressure drop in the channels, and the calculated minor losses for each data point. The average and maximum uncertainties in the experimentally determined frictional pressure drop were 26.6% and 28.9%, respectively. The mean average percent error (MAPE), defined in equation (17),

is 34.8% which is comparable to the maximum uncertainty in the measured frictional pressure drop.

$$MAPE = \frac{100\%}{N} \sum_{i=1}^{N} \left| \frac{\triangle_{P,fric} - \triangle_{P,turb}}{\triangle_{P,fric}} \right| \tag{17}$$

Additionally, to assess if flow mal-distribution could be of significance in the microchannel test sections, the pressure drop in the inlet header was compared against the frictional pressure drop in the microchannels. The pressure drop in the inlet header is mainly associated with the header to channel contraction ("D"). Figure 10 shows the magnitude of these two pressure drops as a function of inlet Reynolds number for the adiabatic test case. On average, the frictional pressure drop in the channels is seven times larger than the pressure drop encountered in the inlet header, therefore flow mal-distribution should not be of concern in the current design of the test section.

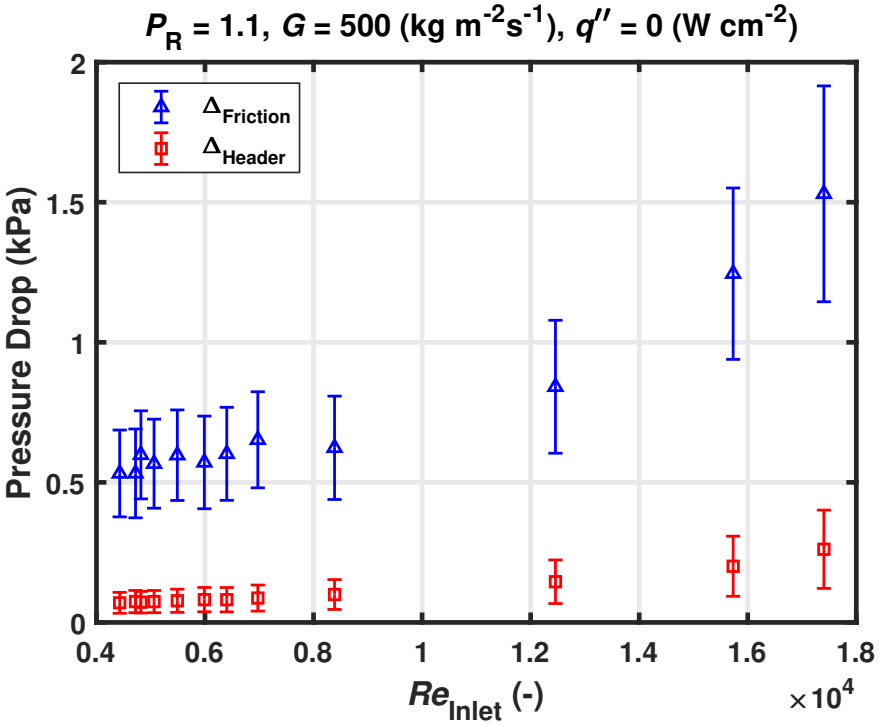

Figure 10: Comparison of the frictional pressure drop in the microchannels (AR = 1) and the pressure drop encountered in the inlet header of the experimental test section.

2.3.4. Wall Shear Stress and Friction Velocity Calculations

Once the frictional pressure drop in the channels was evaluated, the wall shear stress can be calculated as shown by equation (18). This expression results from a force balance done on a fluid element in the fully developed region of the test section. This analysis was not done for the micro-pin array.

$$\frac{\triangle_{P,fric}}{L_{Chan}} = \frac{per}{A_{chan}}(\tau_{w,cpr}) \tag{18}$$

To modify this value for variable property flows, a correction factor, defined in [50] and employed by [51] was used. This expression is represented by equation (19) in which the property ratio terms serve as a correction factor for constant property wall shear stress. This approach is similar to that used in the development of heat transfer correlations for variable property turbulent flows [4].

$$\frac{\tau_{w,vpr}}{\tau_{w,cpr}} = \left(\frac{\rho_w}{\rho_{bulk}}.\frac{\mu_w}{\mu_{bulk}}\right)^{0.18} \tag{19}$$

Once the wall shear stress is known, friction velocity and the length scale associated with the viscous sub-layer in the turbulent boundary layer were evaluated by equation (20) and equation (21), respectively. In evaluating these parameters, the thermophysical properties were evaluated at the channel average bottom wall temperature as the bulk temperature is not representative of the temperature in the near-wall region of the turbulent boundary layer.

$$V^* = \sqrt{\frac{\tau_{w,vpr}}{\rho_w}} \tag{20}$$

$$\delta_{viscous} = \frac{\nu_w}{V^*} \tag{21}$$

3. Results and Discussion

Experiments were conducted for varying inlet temperature ($16 \leq T_{in} \leq 50$ °C), mass flux ($300 \leq G \leq 1000$ kg m^{-2} s^{-1}), heat flux ($20 \leq q'' \leq 40$ W cm^{-2}) and a reduced pressure (P_R) of 1.1. A total of 48 data points were obtained for square channels (aspect ratio of 1) with bottom heating, and 23 for top heating. Thirty four total data points were obtained for aspect ratio of 2, and 8 for the micro-pin array. The average uncertainty in

heat transfer coefficient was 3.4%, 8.03%, and 10.7% for aspect ratio 1, aspect ratio 2, and micro-pin arrays, respectively. The average uncertainty in friction pressure loss were 53.2%, 10.32%, and 5.7%, respectively. For rectangular microchannels with aspect ratio of 1, since the absolute magnitude of the total pressure drop is relatively low, the relative uncertainty associated with the minor losses dominates the uncertainty in frictional pressure drop. All raw and reduced data are available in [52], to allow replication of the results.

In general, it was found that for the experimental conditions of the current study, the heat transfer performance of sCO_2, in rectangular microchannels of aspect ratio 1, was independent of the orientation. An increase in the channel aspect ratio caused an enhancement in heat transfer coefficients along with an increase in pressure drop. The heat transfer performance of the staggered pin array flow geometry was superior to the rectangular channels, but this enhancement in heat transfer was commensurate with the increase in pressure drop. The following sections will provide details and explanations for these observed trends.

3.1. Orientation Effects

For supercritical flows in uniformly heated macroscale, circular, and horizontal flow channels, the potential influence of buoyancy forces on the turbulent thermal transport can be determined by using the semi-empirical criterion proposed by Petukhov and Polyakov [18]. The Grashof number expression (Gr_{th}), defined in equation (22), sets a threshold beyond which buoyant production or destruction of turbulent kinetic energy, due to fluctuating density ($\rho^{'}$), is significant enough to alter the mean velocity and temperature profiles. In particular, the numerical value of the threshold signifies a 1% deviation of the mean velocity and temperature profiles from those of pure forced convective flows. In effect, this criterion captures the structural effect of density fluctuations on turbulence, which is distinct from bulk motion induced by mean density gradients in either laminar or turbulent flows [18].

$$Gr_{th} = 3 \times 10^{-5} Re_{bulk}^{2.75} \bar{Pr} \left[1 + 2.4 Re_{bulk}^{-\frac{1}{8}} \left(\bar{Pr}^{\frac{2}{3}} - 1 \right) \right] \tag{22}$$

$$\bar{Pr} = \frac{h_w - h_{bulk}}{T_w - T_{bulk}} \frac{\mu_{bulk}}{k_{bulk}} \tag{23}$$

The functional form of equation (22) reveals some additional physical insights into the mechanism of density fluctuations interacting with turbulence. The Reynolds number dependence accounts for shear production of turbulence. A large Reynolds number increases the relative contribution of shear production of turbulence as opposed to buoyant production or destruction, thereby increasing Gr_{th}. The integrated Prandtl number ($\bar{Pr}$) in Gr_{th} accounts for the relative thickness of the conduction dominated region of the temperature boundary layer to that of the viscous sub-layer. For a Prandtl number of unity, these thicknesses are approximately the same. It is in this diffusion dominated region of the thermal boundary layer that the steepest density gradients are seen. However, within this region, viscous effects will act to suppress any turbulence produced by density fluctuations. It is at the edge of this region, where there is a reduction in viscous damping, that turbulence kinetic energy is generated. An increase in Prandtl number places the region with the steepest density gradient within the viscous sub-layer. Thus, any turbulence production due to density fluctuations will be damped, explaining an increase in the value of Gr_{th} with an increased Prandtl number.

To relate these structural changers to the mean flow parameters, another non-dimensional number is required. The magnitude of buoyant production or destruction of turbulence due to density fluctuations is proportional to the mean density gradients across the flow channel [53]. The magnitude of mean density gradients is captured by the conventional Grashof number, defined in equation (24) which is based on the channel hydraulic diameter. Therefore, if Gr_q approaches Gr_{th}, or $\frac{Gr_q}{Gr_{th}} > 1$, then density fluctuations will be strong enough to influence turbulent thermal transport [18].

$$Gr_q = \frac{g\bar{\beta}q^{''}D_H^4}{\nu_{bulk}^2 k_{bulk}} \tag{24}$$

$$\bar{\beta} = \frac{1}{\rho_{film}} \frac{\rho_{bulk} - \rho_w}{T_w - T_{bulk}} \tag{25}$$

In recent years, Bazargan *et al.* [16] have used this particular criterion to screen their experimental sCO_2 data for the presence of buoyancy effects. In their experimental investigations on sCO_2 in uniformly heated horizontal test sections when the ratio $\frac{Gr_q}{Gr_{th}}$ was greater

than 1, buoyancy effects were found to be significant, as indicated by a circumferential variation in the tube wall temperatures. This suggests that the Petukhov and Polyakov criterion can be applied to uniformly heated supercritical flows.

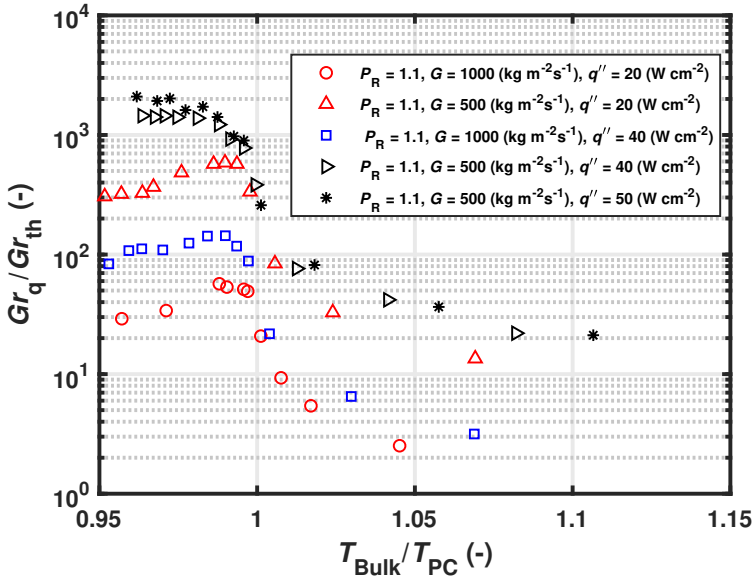

Figure 11: Screening of the experimental data for the presence of buoyancy effects by using the criterion proposed by [18] for a microchannel test section with an aspect ratio of 1.

Figure 11 shows the ratio $\frac{Gr_q}{Gr_{th}}$ for all of bottom heated data in the square (AR = 1) microchannel from this study. The results predict that all data in this study should be influenced by buoyancy. However, both the threshold criterion and the Grashof number defined in equation (24) are applicable for uniformly heated circular geometries, and therefore potentially unsuitable for the non-uniformly heated, non-circular geometries considered here.

To empirically assess the potential importance of buoyancy, experiments are conducted with the test section inverted, yielding a top heated boundary condition for horizontal flow. Top heated configuration will potentially result in stable stratification at the flow channel wall as opposed to potential unstable stratification for bottom heated configuration. Any difference in the calculated average heat transfer coefficients will confirm that there is indeed stratification in the flow channel and hence buoyancy effects on heat transfer cannot be

ignored.

A similar approach was used by Hauptmann [54] in a study to measure and visualize the heat transfer behavior of sCO_2 over a bottom heated flat plate. By analysis of the visual data, it was established that significant density gradients (stratification) were present across the boundary layer. The heat transfer coefficients for the top heated configuration were compared to those for bottom heated configuration of the test section. For experimental conditions, when heat transfer coefficients were dependent upon the orientation of the test section, buoyancy effects were deemed significant.

At this point, it is essential to point out that the current test section was never purely heated through top or bottom heating due to heat leakage through the diffusion bonded region, as revealed by the the 3-D data analysis procedure described in Section 2.3.1. For instance, 17% of the total heat duty for a bottom applied heat flux of 40 W cm^{-2} heats the fluid channels from the top. Despite this, if there is any stratification in the channels to begin with, changing the orientation of the test section will confirm it.

Experiments with top heating were conducted for the test cases listed below. These conditions were chosen as the most likely to be influenced by buoyancy because the magnitude of the ratio, $\frac{Gr_q}{Gr_{th}}$ was highest among all of the test cases.

1. $P_R = 1.1$, $G = 500$ kg m^{-2} s^{-1} and $q'' = 40$ W cm^{-2}
2. $P_R = 1.1$, $G = 500$ kg m^{-2} s^{-1} and $q'' = 50$ W cm^{-2}

Figure 12 shows the comparison of heat transfer coefficients for the two heat transfer orientations of the microchannel test section with an aspect ratio of 1. For both of the test cases, the majority of data points for the two orientations are within experimental uncertainty and no general orientation dependent trend is apparent. This suggests that buoyancy effects for these particular geometries are negligible.

Two possible explanations are that the Grashof number (Gr_q) is being overestimated by assuming that applied heat flux, q'', is uniform across the perimeter of the flow channel and that D_h is not the appropriate characteristic length scale across which the density gradients exist. This leads to a potentially false conclusion that density gradients are significant

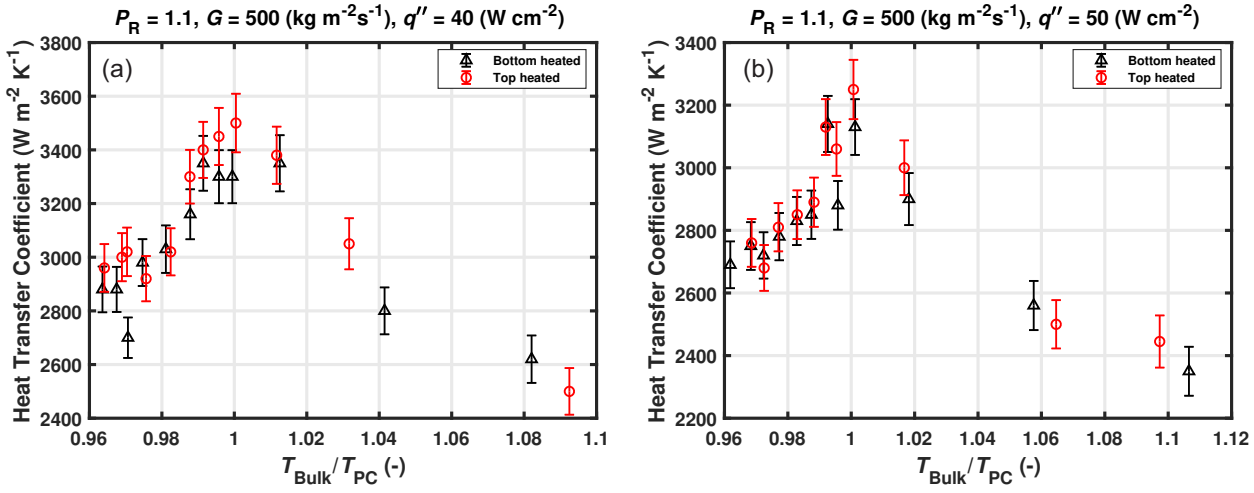

Figure 12: Comparison of the heat transfer coefficients for two different orientations for a microchannel test section with an aspect ratio of 1. (a) Applied heat flux of 40 W cm^{-2}. (b) Applied heat flux of 50 W cm^{-2}.

enough to alter turbulence production or destruction. Therefore, the ratio $\frac{Gr_q}{Gr_{th}}$ as proposed by Petukhov and Polyakov [18] should not be used to design devices with these operating conditions. This conclusions is strengthened by the analysis below showing that density gradients are not strong enough to alter turbulent production or dissipation in the boundary layer.

For turbulent mixed convection in channels, the ratio of turbulence production due to buoyancy forces and the shear forces is called the flux Richardson number (R_F) and is defined as shown in equation (26). This expression assumes that the velocity profile in the channel is logarithmic and that the shear stress and heat flux are constant in the near wall region of the turbulent boundary layer (Couette flow approximation) [55, 3]. When the thermal transport is upward (positive y axis - upright orientation), this number is negative, and vice versa.

$$R_F = \frac{0.5 D_h q''_{av} \kappa g}{\rho c_p T_{wall,K} V^{*3}} \tag{26}$$

$$q''_{av} = \alpha (T_w - T_{bulk}) \tag{27}$$

Petukhov and Polyakov, in their text [18], recommend a critical value of ± 0.042 for the flux Richardson number. For stable or unstable stratification, if the absolute value of R_F

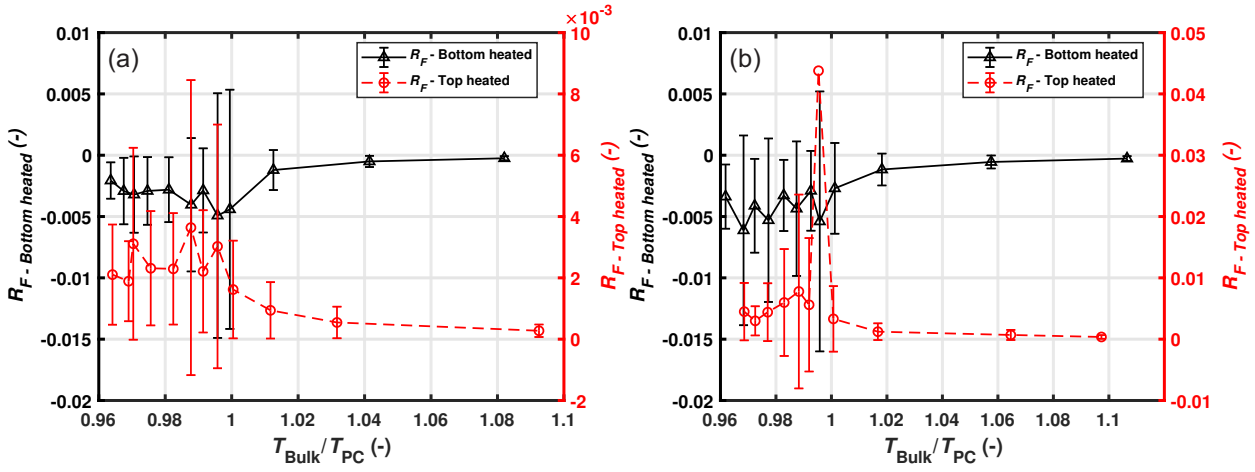

Figure 13: Flux Richardson number of the microchannel based test section with an aspect ratio of 1 for two different orientations. (a) P_R = 1.1 , G = 500 kg m^{-2} s^{-1}, q" = 40 W cm^{-2}. (b) P_R = 1.1 , G = 500 kg m^{-2} s^{-1}, q" = 50 W cm^{-2}. The uncertainty bars on the data points represent the uncertainty that propagates into the calculation of the flux Richardson number from the measured frictional pressure drop.

exceeds 0.042, buoyancy effects on turbulence, and therefore on thermal transport, cannot be ignored. Figure 13 shows the values of the flux Richardson number (R_F) for bottom and top heated orientations of the test section for two different set of experimental conditions. For both of the test conditions, R_F never exceeds 0.042 except for one data point, seen in Figure 13 (b) for inverted orientation. This implies that any effects of stable stratification on turbulent transport can be ignored.

Additionally, for stable stratification in plane turbulent Couette flows, the ratio of the length scales associated with buoyancy and near wall viscous length scale reveals if buoyancy effects are significant to suppress turbulence [56]. This ratio is defined in equation (28), where L_{buoy} is the *Monin-Obukhov* length scale [57]. The near wall viscous length scale, associated with the decay of turbulent kinetic energy, is defined in equation (21). The value of L^+ needs to stay above 200 for the flow to stay fully turbulent [56]. As seen in Figure 14, L^+ never drops down for either of the test cases. This implies that the length scale associated with buoyancy, relative to viscous lengths scale, is not small enough to damp the turbulent kinetic energy.

$$L^+ = \frac{L_{buoy}}{\delta_{viscous}} \tag{28}$$

$$L_{buoy} = \frac{T_{w,K} V^{*3} \rho_w c_{p,w}}{\kappa g q''_{av}} \tag{29}$$

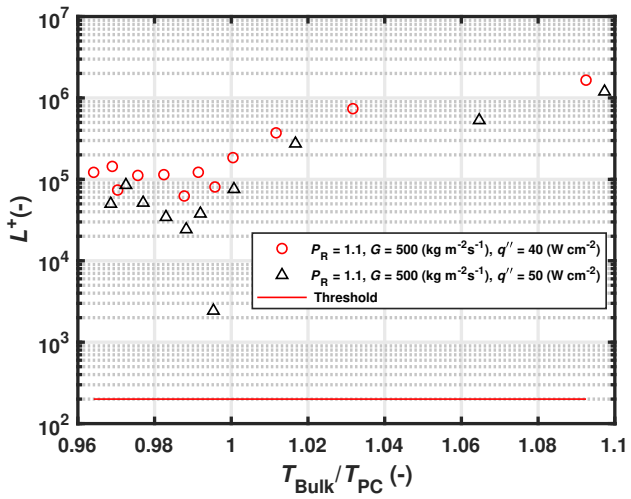

Figure 14: L^+ values for the top heated configuration of the microchannel test section with a channel aspect ratio of 1.

For the bottom heated orientation of the test section, the value of R_F never exceeding 0.042 implies that the structural effect of density fluctuations on turbulence can be ignored [18]. However, it can still be argued that sharp density gradients will still induce some bulk fluid motion normal to the wall in the form of rising thermal plumes as observed in the recent numerical investigation by Nabil and Rattner [23]. They conducted a computational investigation based on the microchannel geometry of aspect ratio 1 in the current investigation. Large Eddy Simulations (LES) of the flow channel revealed significant density gradients within the boundary layer, causing the formation of thermal plumes at the bottom wall. It is therefore valuable to do some additional analysis which compares the magnitude of this bulk fluid motion to that associated with turbulent shear transport.

The characteristic velocity of eddies transporting heat and momentum normal to the heated surface due to the shear can be approximated by the friction velocity. The characteristic velocity associated with the buoyancy force is approximated by using the momentum differential due to density gradients in the conduction dominated region of the turbulent boundary layer. It is in this region that the steepest temperature and therefore the steepest density gradients for supercritical fluids exist. This is shown schematically in Figure 15

(a). The thickness of the conduction dominated region of the turbulent boundary layer is defined in equations (30) to (31) [3]. In these calculations, the non-dimensional thickness of the viscous sub-layer region , $\delta^+_{viscous}$ is assumed to be 5 [3, 4]. The characteristic velocity then, normal to the heated wall, resulting due to this density gradient, is represented by equation (32).

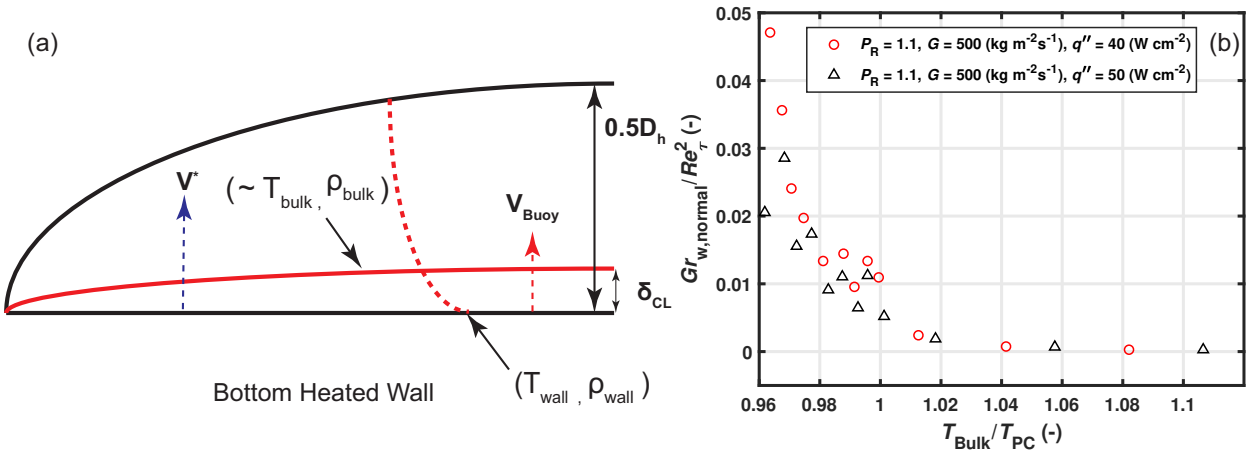

Figure 15: (a) Schematic of the turbulent boundary layer. Transport in the near wall region (δ_{cl}) is diffusive, thereby leading to a steep temperature gradient. This temperature gradient will establish a density gradient across the conduction layer, inducing a velocity normal to the heated wall (V_{Buoy}). (b) Comparison of the wall normal momentum transport associated with the density gradients and shear in the boundary layer.

$$\delta^+_{cl} = \frac{\delta^+_{viscous}}{Pr_w^{\frac{1}{3}}} \tag{30}$$

$$\delta_{cl} = \delta^+_{cl}\delta_{viscous} \tag{31}$$

$$V_{buoy} = \sqrt{g\beta_{film}\delta_{cl}(T_w - T_{bulk})} \tag{32}$$

Once the characteristic velocity due to the mean density gradients is known, it is non-dimensionalized by evaluating a Grashof number based on this velocity. The expression used to calculate this is shown in equation (33). The magnitude of this wall normal Grashof number is compared to the friction Reynolds number, $Re_\tau = \frac{V^* 0.5 D_h}{\nu_w}$. The friction Reynolds number represents the momentum transport normal to the wall by eddies generated due to

shear mechanism.

$$Gr_{w,normal} = \left(\frac{V_{buoy} 0.5 D_h}{\nu_w}\right)^2 \tag{33}$$

The ratio, $\frac{Gr_{w,normal}}{Re_\tau^2}$ is plotted in Figure 15 (b). For bulk fluid motion induced by density gradients to be a significant contributor to the thermal and momentum transport, this ratio should be ≥ 1. As shown in Figure 15 (b), this ratio never exceeds 0.05. Therefore, it can be concluded that for the bottom heated orientation of the test section, both the structural and changes to the mean flow, a consequence of variable fluid density can be ignored. This conclusion goes against the predictions of the criterion of evaluating the ratio $\frac{Gr_q}{Gr_{th}}$, proposed by Petukhov and Polyakov [18], when applied to the current design of the experimental test section. The reason, as mentioned earlier, is attributed to the fact that the magnitude of the conventional Grashof number (Gr_q) is being overestimated due to the non-uniformity of the applied heat flux and assuming the channel hydraulic diameter as the length scale across which the steepest density gradient exists.

At this point, it is also imperative to mention that this analysis was done by using constant average channel wall temperatures and heat flux. Therefore, this analysis cannot resolve the significance of buoyancy on thermal transport on a local scale. This is especially true for the channel length corresponding to the directly heated region of the test section. In this particular portion of the test section, the local Rayleigh number, based on the thickness of the conduction region, can be of the order 10^3. This will then lead to the formation of thermal plumes as observed in the the numerical investigation of Nabil and Rattner [23]. Higher resolution heat transfer data is required to identify such effects in the current experimental study.

3.2. Channel Aspect Ratio Effects

The heat transfer and pressure drop results for the microchannel based test sections of aspect ratios 1 and 2 are presented in Figure 16.

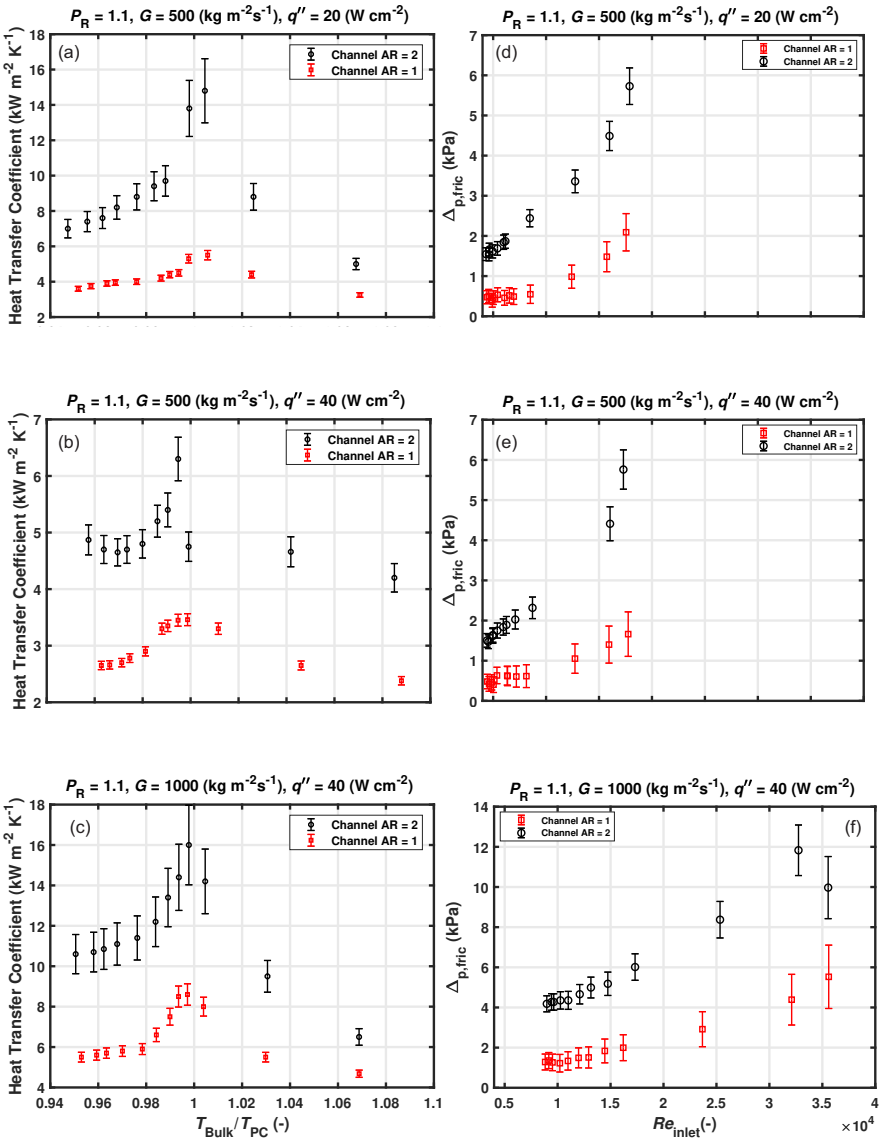

Figure 16: (a)-(c)Heat transfer coefficients versus the ratio of bulk to pseudo-critical temperature and (d)-(e) frictional pressure drop for different aspect ratios.

For both the microchannel test sections, the heat transfer coefficients exhibit a peak when the bulk fluid temperature approaches the pseudo-critical temperature. This is attributed to favorable thermophysical properties in the boundary layer as described in [24]. An increase in the mass flux leads to an increase in the heat transfer coefficients for both of the test sections which is inline with the observations from single phase heat transfer theory.

Additionally, for a fixed mass flux, an increase in the applied heat flux leads to a reduction in the magnitude of the heat transfer coefficients. This is due to poorer thermophysical properties in the diffusion dominated region at higher heat fluxes. For supercritical heat transfer in uniformly heated geometries, this degradation in heat transfer can also happen due to buoyancy or flow acceleration effects. However, as established in section 3.1, bulk buoyancy effects on heat transfer were not present. Flow acceleration may be affecting the experimental data. Higher resolution heat transfer data is required to answer this definitively.

The frictional pressure drop, for the range of experimental conditions investigated here, increased with an increase in the channel aspect ratio. This increase in the pressure drop can be explained by presence of secondary flow patterns near the channel corners as the aspect ratio increases [58] and an increase in the near wall velocity fluctuations, i.e. Reynolds shear stress [31]. Increase in the magnitude of the correlated velocity fluctuations will enhance the turbulent thermal transport, thereby causing an increase in the the heat transfer coefficients for rectangular channels with aspect ratio of 2 as seen in Figure 16 (a) - (c).

It is also of interest to compare the ratio of frictional pressure drop to pressure drop associated with the bulk fluid acceleration for the two different aspect ratios. For turbulent flows, Reynolds shear stress is the biggest contributor to the overall shear stress. This stress results due to momentum transport normal to the channel wall due to correlated velocity fluctuations [55]. On the other hand, acceleration pressure drop, associated with the axial momentum change, acts parallel to the flow direction. If the acceleration pressure drop is significantly larger than the Reynolds shear stress, it can suppress ejection events in the turbulent boundary layer [4, 7, 6, 3], thereby reducing turbulent transport normal to the channel wall. Therefore, a comparison of the magnitudes of the acceleration pressure drop

and the frictional pressure drop will reveal which geometry has higher tendency to be affected by flow acceleration effects.

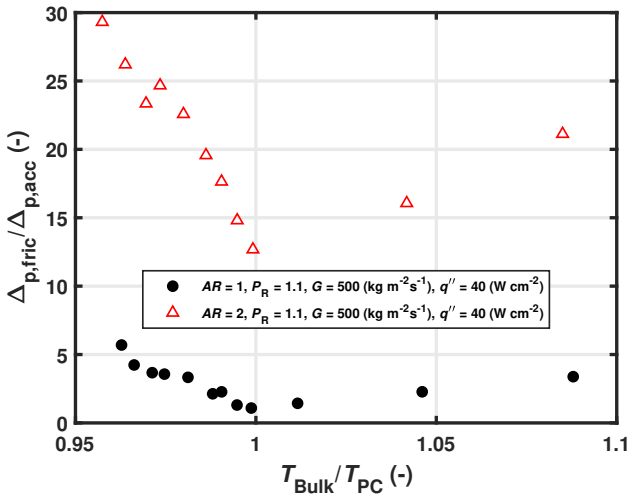

Figure 17: Ratio of frictional and acceleration pressure drop as a function of channel aspect ratio. Aspect ratio 1 channels, in the proximity of the pseudo-critical point, show a higher tendency of being potentially affected by bulk flow acceleration.

The experimental conditions with the lowest mass flux and the highest applied heat flux are in general more prone to be affected by flow acceleration effects [20, 11, 10]. Therefore the pressure ratios for the test case with a mass flux of 500 kg m $^{-2}$ s^{-1} and an applied heat flux of 40 W cm^{-2} were chosen for this comparison. As shown in Figure 17, for microchannel test section with an aspect ratio of 1, in the proximity of the pseudo-critical point, the ratio of acceleration to frictional pressure drop is nearly unity. This suggests that turbulent transport could be affected for this channel geometry for conditions that span the pseudo-critical point. However, for the test section with an aspect ratio of 2, the pressure ratio never drops below 10 and therefore, for these particular conditions, the likelihood of suppression in turbulent transport due to a favorable pressure gradient is reduced.

3.3. Micro-pin Flow Passages

Preliminary results for the micro-pin flow passages were reported in [33]. This work is expanded in this section by reporting frictional pressure drop, additional comparison of the experimental data with literature correlations, and a comparison with microchannels of aspect ratio 2 at similar operating conditions. The heat transfer coefficients associated with the micro-pin based test section are presented in Figure 18 (a). The choice of data set, in particular the mass flux, that is presented here for the micro-pin test section is influenced by the maximum experimental uncertainty. The very high convective heat transfer coefficients in the micro-pin array leads to a small bulk-to-wall temperature difference and unacceptable uncertainty for many conditions using the present test section design. Thus, only results with a mass flux of 315 kg m^{-2} s^{-1}, which resulted in reasonable experimental uncertainty, are presented here.

Figure 18 (a) shows that as expected, the heat transfer coefficients were highest when the pseudo-critical temperature occurs within the thermal boundary layer ($T_{Bulk} \leq T_{PC} \leq T_w$). Subsequently, the heat transfer coefficient decreases as the bulk temperature increases beyond the pseudo-critical temperature. Figure 18 (a) also shows that the heat transfer coefficients for the pin array, when the ratio $T_{Bulk}/T_{PC} < 1$, are on average twice than those for the microchannel heat exchanger with an aspect ratio of 2. This is despite the fact that the mass flux in the microchannel based geometries is approximately 66 % higher than that in the pin array. However, this improved heat transfer in the pin array carries a commensurate penalty in pressure drop, as shown in Figure 18 (b).

Also shown in Figure 18 (c) is friction factor versus the Reynolds number for three different geometries. The Reynolds number and the velocity used to evaluate the friction factor in the micro-pin array is based on the minimum flow area whereas, for the microchannel based geometries, inlet Reynolds number, based on the channel hydraulic diameter, was used. Density was evaluated as a function of test section inlet absolute pressure and the average of the inlet and exit temperatures of the flow channels. It is important to mention that the fluid properties, bulk flow velocity and friction factor are changing along the flow length for the heated cases. This makes it difficult to draw definite conclusions or directly compare

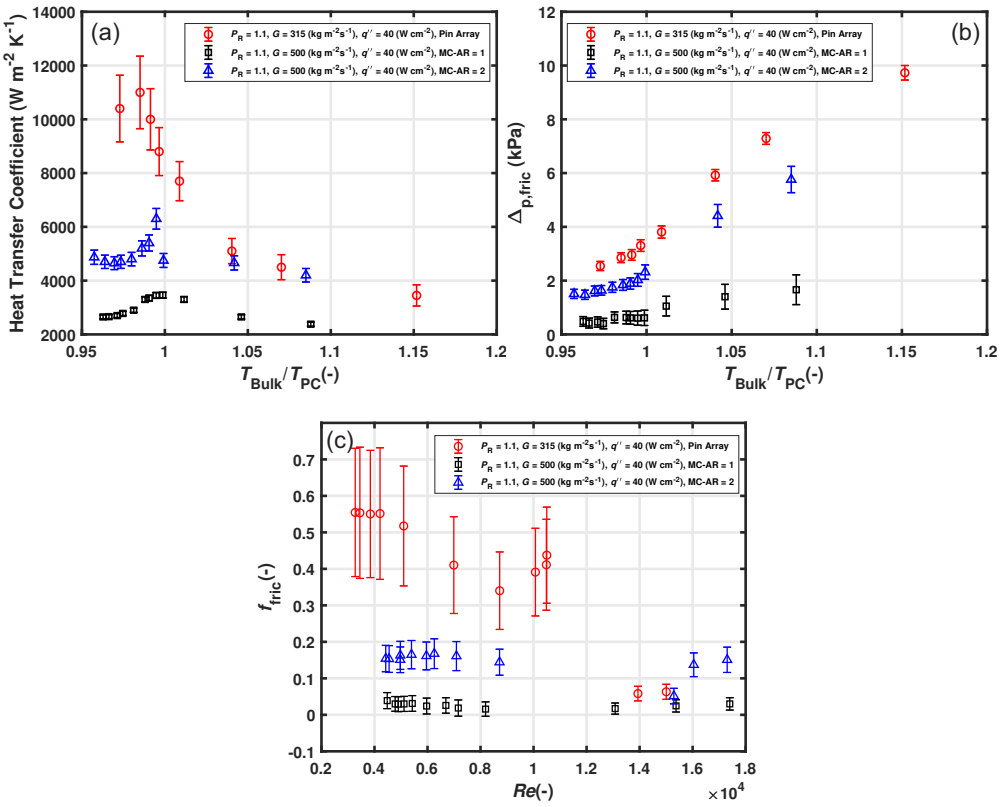

Figure 18: Heat transfer coefficients, frictional pressure drop, and friction factor comparison for micro-pin and microchannel based geometries. (a) Heat transfer coefficient comparison. (b) Frictional pressure drop comparison. (c) Friction factor versus the Reynolds number for three different geometries.

one case to another. The measured frictional pressure drop is therefore more representative of the actual flow resistance in the flow passages for the near-critical heated flows.

Nonetheless, in general, the friction factor for the microchannel flow passages is independent of the Reynolds number. This is consistent with single phase turbulent flow in fully rough flow situations [45]. The minor deviations in the trend can be explained due to axial variations of the velocity in the flow channels due to changing density which are not captured in the calculations using the inlet/bulk fluid density. For the pin array, in general, the friction factor exhibits a dependence on Reynolds number of the form, $f_{fric} \propto Re^{-x}$, where x is a constant. Using air as a working fluid, Jeng and Tzeng arrived at a similar correlation for the friction factor data in staggered square pin-fin array[59].

Experimental heat transfer data for the micro-pin test section were also compared to

the predictions of some correlations available in the literature. In general, most of the correlations available in the literature are for laminar flow. Three correlations that are potentially applicable for the turbulent flow through cylinders/pins are summarized in Table 4. The correlation by Rasouli *et al.* was developed for Reynolds numbers ranging from 8 to 1169 which are lower than the Reynolds numbers for the current micro-pin test section (4319 to 13852, based on the hydraulic diameter). The reason this correlation is chosen for comparison against the current data is because of the similarity in the geometry used.

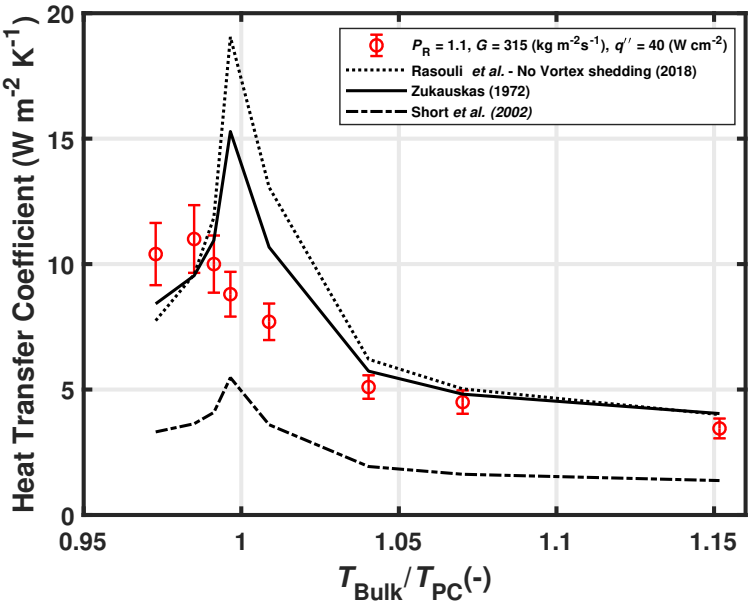

Figure 19: Comparison of the experimental data for the micro-pin test section with the predictions of correlations.

Figure 19 shows the experimental results and the predictions of the three correlations as a function of bulk-to-pseudo critical temperature ratio. The MAPE for each correlation is tabulated in Table 4 for data below the pseudo critical temperature, in the vicinity of the pseudo critical temperature and higher than the pseudo critical temperature. Despite being developed for larger geometries, the Zukauskas [39] correlation was able to predict the experimental data best for all three regimes with an average MAPE of 23.8 %. The correlation proposed by Rasouli *et al.* for single phase flows in staggered pin arrays was able to predict the experimental data with a MAPE of 13.8% when the ratio, $\frac{T_{Bulk}}{T_{PC}}$ exceeded

Table 3: Details of the correlations used for comparison against experimental data for the micro-pin test section.

Authors	Correlation	Conditions/Comments
Zukauskas [39]	$Nu_{D_h} = 0.35\left(\frac{\beta_T}{\beta_L}\right)^{0.2} Re_{D_h}^{0.6} Pr^{0.36} \left(\frac{Pr}{Pr_{wall}}\right)^{0.25}$	$10^3 \leq Re_{D_h} \leq 2 \times 10^5$ $0.7 \leq Pr \leq 500$ $\frac{\beta_T}{\beta_L} < 2$ Tube bank Staggered circular tube All fluids
Short *et al.* [40]	$Nu_{D_h} = 0.419\left(\frac{H_{pin}}{D_h}\right)^{-0.3} \left(\frac{S_L}{D_h}\right)^{0.077} \left(\frac{S_T}{D_h}\right)^{0.2} Re_{D_h}^{0.45} Pr^{\frac{1}{3}}$	$Re_{D_h} > 1000$ Macro pin fin heat sink Staggered circular pin $1.9 < \frac{H_{pin}}{D_h} < 7.2$ $2.0 < \frac{S_T}{D_h} < 6.4$ $1.8 < \frac{S_L}{D_h} < 3.2$
Rasouli *et al.* [41]	$Nu_{A_{min},noVS} = 0.039\left(\frac{S_T - D_h}{D_h}\right)^{-0.19} Re_{A_{min}}^{0.837} Pr^{0.557}$	Micro-pin heat sink No vortex shedding Staggered diamond pin fins Liquid Nitrogen and PF-5060 $0.7 < \frac{H_{pin}}{D_h} < 3.2$ $1.7 < \frac{S_T}{D_h} < 3.0$ $0.8 < \frac{S_L}{D_h} < 1.5$

unity. The worst agreement of the experimental data was with the correlation proposed by Short *et al.* [40].

The Zukauskas [39] correlation was able to predict the experimental data, with reasonable accuracy, because the geometric parameters as specified by the ratio, $\frac{\beta_T}{\beta_L}$ are similar to the current design of the experimental test section. A similar line of reasoning can be used to explain the poor agreement of the experimental data with the correlation of Short *et al.* [40], where the geometric dimensions for which the correlation was developed for were larger than those in the current experimental test section. In particular, for the current test section , the ratios, $\frac{H_{pin}}{D_h}$, $\frac{S_T}{D_h}$ and $\frac{S_L}{D_h}$ were 0.59, 2.23 and 1.107, respectively. As can be seen in Table 3, these ratios are either equal to or lower than the minimum values of

Table 4: *MAPE* values for the comparison of the experimental data for the micro-pin test section against the predictions of the correlations.

	T_b/T_{PC}	Rasouli *et al.* [41]	Zukauskas [39]	Short *et al.* [40]
	< 0.99	19.15	16.17	67.5
	0.99 - 1.01	56.6	33.5	53.05
	> 1.01	13.8	12.1	62.05
Average		36.5	23.8	58.9

these parameters for which the correlation proposed by Short *et al.* is applicable. Closely spaced pins are expected to provide better heat transfer performance but with a penalty of increased pressure drop.

4. General Recommendations

Some general design recommendations for supercritical carbon dioxide thermal management devices can be made from the results of this study.

1. For applications, involving high heat fluxes ($\geq$ 50 W cm^{-2}), and low mass fluxes ($\leq$ 500 kg m^{-2} s$_{-1}$), microchannel devices with higher aspect ratios are preferred over square (AR = 1) channels. This is due to the fact that potential heat transfer degradation due to flow acceleration is likely to be reduced in higher aspect ratio channels, as shown in section 3.2.
2. If the designer is not worried about the pumping costs or the overall coefficient of performance of the cooling system, then micro-pin based geometries are preferred over microchannel based geometries. Qualitatively, this recommendation is in line with the observations from the conventional, constant property, single-phase turbulent heat transfer theory. Quantitative difference might stem from local buoyancy, flow acceleration, and variable property effects. Local heat transfer data is required to investigate those effects.

3. For the current design of heat sinks, with aspect ratio of 1, buoyancy effects were not found to affect heat transfer. Therefore, for similar geometries and for similar heating boundary conditions, the operation orientation should not be of concern to the designer. However, this recommendation might not hold true if the channel dimensions or the spatial distribution and magnitude of the applied heat flux were to change in any manner. Further work is required in this area.

5. Conclusions

The main objective of this investigation was to characterize the thermal-hydraulic performance of sCO_2 as a function of channel flow geometry and heat exchanger orientation. These experiments were conducted for non-uniform heat flux boundary conditions, mimicking the operating conditions encountered in thermal management applications.

Three different geometries were investigated. Two of these had microchannel flow passages of the same hydraulic diameter, 750 μm, but the channel aspect ratio varied between these test sections. The third test section had a staggered array of micro-pins forming the flow passage with a hydraulic diameter of 679 μm. Data were collected for inlet temperature ($16 \leq T_{in} \leq 50$ °C), mass flux ($315 \leq G \leq 1000$ kg m^{-2} s^{-1}), heat flux ($20 \leq q'' \leq 40$ W cm^{-2}) and reduced pressure (P_R) of 1.1. A data analysis method developed in Jajja *et al.* [24] using a combination of 2-D and 3-D heat transfer models of the test section was used to calculate the average heat transfer coefficients. Additionally, pressure drop models were also developed to isolate the frictional pressure drop in the flow channels.

The results indicated that the performance of the microchannel based heat exchanger with a channel aspect ratio of 1 is orientation independent. This conclusion is based on operating the test section in a upright and inverted orientation. Additional analysis, based on the average heat transfer data, also revealed that buoyancy's effect on thermal transport can be ignored for this particular test section. However, heat transfer data with a high spatial resolution is required to assess the influence of buoyancy on a local scale.

Increase in the channel aspect ratio, for microchannel based test sections, resulted in an enhancement in both thermal and momentum transport for bottom heated horizontal

orientation. It was also found that an increase in channel aspect ratio can negate possible flow acceleration effects for equivalent mass flux and applied heat flux.

For one particular set of experimental conditions, the thermal-hydraulic performance of the staggered pin array flow geometry was compared with the microchannel based geometries. In this comparison, the heat transfer performance of the staggered pin array flow geometry was the best but this enhancement in heat transfer carried a commensurate penalty in pressure drop. Additionally, the experimental data for the micro-pin array test section was also compared against the predictions of correlations available in the literature. The correlation proposed by Zukauskas was able to capture the overall trends in heat transfer data with an average MAPE of 23.8%.

6. Acknowledgements

This material is based upon work supported by the National Science Foundation under Grant No. 1604433.

References

[1] B. M. Fronk, A. S. Rattner, High-Flux Thermal Management With Supercritical Fluids, Journal of Heat Transfer 138 (2016) 124501.

[2] O. C. da Rosa, F. G. Battisti, G. M. Hobold, A. K. da Silva, Enhancing Heat Rejection From Electronic Devices With a Supercritical Carbon Dioxide Minichannel Heat Exchanger, International Journal of Refrigeration 106 (2019) 463–473.

[3] P. Davisdon, Turbulence : An Introduction for Scientists and Engineers, Oxford University Press, 2 edition, 2015.

[4] W. M. Kays, M. Crawford, Convective Heat and Mass Transfer, McGraw-Hill, 2 edition, 1980.

[5] K. R. Perkins, Turbulence structure in gas flows relaminarizing by heating, Ph.D. thesis, University of Arizona, 1975.

[6] S. J. Kline, W. C. Reynolds, F. A. Schraub, P. W. Runstadler, The structure of turbulent boundary layers, Journal of Fluid Mechanics 30 (1967) 741–773.

[7] J. R. Harris, B. W. Lance, B. L. Smith, Experimental Validation Data for Computational Fluid Dynamics of Forced Convection on a Vertical Flat Plate, Journal of Fluids Engineering 138 (2015) 011401.

[8] V. Patel, M. Head, Reversion of turbulent to laminar flow, Journal of Fluid Mechanics 34 (1968) 371–392.

[9] J. Wang, J. Li, J. D. Jackson, A study of the influence of buoyancy on turbulent flow in a vertical plane passage, International Journal of Heat and Fluid Flow 25 (2004) 420–430.

[10] J. D. Jackson, Fluid flow and convective heat transfer to fluids at supercritical pressure, Nuclear Engineering and Design 264 (2013) 24–40.

[11] J. D. Jackson, Models of heat transfer to fluids at supercritical pressure with influences of buoyancy and acceleration, Applied Thermal Engineering 124 (2017) 1481–1491.

[12] T. Tsuji, Y. Nagano, Velocity and temperature measurements in a natural convection boundary layer along a vertical flat plate, Experimental Thermal and Fluid Science 2 (1989) 208–215.

[13] T. Tsuji, Y. Nagano, Turbulence measurements in a natural convection boundary layer along a vertical flat plate, International Journal of Heat and Mass Transfer 31 (1988) 2101–2111.

[14] K. Theologou, R. Mertz, E. Laurien, J. Starflinger, An Assessment of the criteria for the onset of heat transfer deterioration with supercritical CO2 in vertical heated sigle circular tubes, in: 3rd European supercritical CO2 Conference (2019), Paris.

[15] S. R. Pidaparti, J. A. McFarland, M. M. Mikhaeil, M. H. Anderson, D. Ranjan, Investigation of Buoyancy Effects on Heat Transfer Characteristics of Supercritical Carbon Dioxide in Heating Mode, J. Nuclear Engineering and Radiation Science 1 (2015) 1–10.

[16] M. Bazargan, D. Fraser, V. Chatoorgan, Effect of Buoyancy on Heat Transfer in Supercritical Water Flow in a Horizontal Round Tube, Journal of Heat Transfer 127 (2005) 897.

[17] G. Adebiyi, W.B. Hall, Experimental Investigation of Heat Transfer to supercritical pressure carbon dioxide in a horizontal pipe, International Journal of Heat and Mass Transfer 19 (1976) 715–720.

[18] B. Petukhov, A. Polyakov, Heat Transfer in Turbulent Mixed Convection, Hemisphere Publishing Corporation, 1988.

[19] J. Wang, Z. Guan, H. Gurgenci, K. Hooman, A. Veeraragavan, Computational investigations of heat transfer to supercritical CO 2 in a large horizontal tube, Energy Conversion and Management 157 (2018) 536–548.

[20] J. D. Jackson, Heat transfer deterioration in tubes caused by bulk flow acceleration due to thermal and frictional influences (2012) 223–230.

[21] J. D. Jackson, Screening and Correlating Data on Heat Transfer to Fluids at Supercritical Pressure, Journal of Nuclear Engineering and Radiation Science 2 (2015) 011001.

[22] D. M. McEligot, J. D. Jackson, "Deterioration" criteria for convective heat transfer in gas flow through non-circular ducts, Nuclear Engineering and Design 232 (2004) 327–333.

[23] M. Nabil, A. S. Rattner, Large eddy simulations of high-heat-flux supercritical CO2 convection in

microchannels: Mixed convection and non-uniform heating, International Journal of Heat and Mass Transfer 145 (2019) 118710.

[24] S. A. Jajja, K. R. Zada, B. M. Fronk, Experimental investigation of supercritical carbon dioxide in horizontal microchannels with non-uniform heat flux boundary conditions, International Journal of Heat and Mass Transfer 130 (2019) 304–319.

[25] J. H. Ryu, D. H. Choi, S. J. Kim, Three-dimensional numerical optimization of a manifold microchannel heat sink, International Journal of Heat and Mass Transfer 46 (2003) 1553–1562.

[26] X. Wei, Y. Joshi, Optimization study of stacked micro-channel heat sinks for micro-electronic cooling, Inter Society Conference on Thermal and Thermomechanical Phenomena in Electronic Systems, ITHERM (2002) 441–448.

[27] R. Knight, J. Hall, J. Goodling, C. Jaeger, Heat Sink Optimization with Application to Microchannels, IEEE Transcactions on Components, Hybrids , and Manufacturing Technology 15 (1992).

[28] S. Kakac, K. R. SHah, W. Aung, Handbook of Single-Phase Convective Heat Transfer, John Wiley & Sons, 1987.

[29] X. F. Peng, G. P. Peterson, Convective heat transfer and flow friction for water flow in microchannel structures, International Journal of Heat and Mass Transfer 39 (1996) 2599–2608.

[30] G. Nellis, S. A. Klein, Heat Transfer, Cambridge University Press, 2012.

[31] H. Li, M. G. Olsen, Aspect Ratio Effects on Turbulent and Transitional Flow in Rectangular Microchannels as Measured With MicroPIV, Journal of Fluids Engineering 128 (2006) 305.

[32] O. C. Jones, An Improvement in the Calculation of Turbulent Friction in Rectangular Ducts, Journal of Fluids Engineering 98 (1976) 173–180.

[33] S. A. Jajja, J. M. Sequeira, B. M. Fronk, Experimental Investigation of Supercritical Carbon Dioxide in Horizontal Micro Pin Arrays with Non-uniform Heat Flux Boundary Conditions, in: 4th Thermal and Fluids Conference. April 14-17, 2019, Las Vegas, NV, USA.

[34] A. Koşar, Y. Peles, Thermal-Hydraulic Performance of MEMS-based Pin Fin Heat Sink, Journal of Heat Transfer 128 (2006) 121.

[35] Y. Peles, A. Koşar, C. Mishra, C. J. Kuo, B. Schneider, Forced convective heat transfer across a pin fin micro heat sink, International Journal of Heat and Mass Transfer 48 (2005) 3615–3627.

[36] R. S. Prasher, J. Dirner, J.-Y. Chang, A. Myers, D. Chau, D. He, S. Prstic, Nusselt Number and Friction Factor of Staggered Arrays of Low Aspect Ratio Micropin-Fins Under Cross Flow for Water as Fluid, Journal of Heat Transfer 129 (2007) 141.

[37] W. Qu, A. Siu-Ho, Liquid single-phase flow in an array of micro-pin-finspart I: Heat transfer characteristics, Journal of Heat Transfer 130 (2008) 1–11.

[38] E. Rasouli, V. Narayanan, Single-Phase Cryogenic Flow and Heat Transfer Through Microscale Pin

Fin Heat Sinks, Heat Transfer Engineering 37 (2016) 994–1011.

[39] A. Zukauskas, Heat Transfer from Tubes in Crossflow, Advances in Heat Transfer 8 (1972) 93–160.

[40] B. E. Short, P. E. Raad, D. C. Price, Performance of Pin Fin Cast Aluminum Coldwalls, Part 2: Colburn j-Factor Correlations, Journal of Thermophysics and Heat Transfer 16 (2002) 397–403.

[41] E. Rasouli, C. Naderi, V. Narayanan, Pitch and aspect ratio effects on single-phase heat transfer through microscale pin fin heat sinks, International Journal of Heat and Mass Transfer 118 (2018) 416–428.

[42] COMSOL AB, COMSOL Multiphysics v. 5.1./5.2., 2016.

[43] S. Klein, F-Chart Software: EES, V10.104, 2016.

[44] Crane, Flow of Fluids through Valves, Fittings and pipe, New York, technical edition, 1977.

[45] F. M. White, Fluid Mechanics, McGraw-Hill, 5th edition, 2003.

[46] K. R. Zada, Experimental Investigation of Supercritical Heat Transfer of Carbon Dioxide in Parallel Square Microchannels with a Single-Wall Constant Heat Flux Boundary Condition., Oregon State University MS Thesis (2017).

[47] S. Garimella, A. Agarwal, B. M. Fronk, The intermittent and annular flow condensation continuum: Pressure drops at the microscale, International Journal of Multiphase Flow 84 (2016) 129–144.

[48] A. Agarwal, S. Garimella, Representative Results for Condensation Measurements at Hydraulic Diameters 100Microns, Journal of Heat Transfer 132 (2010) 041010.

[49] S. W. Churchill, Friction-factor equation spans all fluid flow regimes, 1977.

[50] V. G. Razumovskiy, A. P. Ornatskiy, Y. M. Mayevskiy, Local Heat Transfer and Hydraulic Behavior in Turbulent Channel Flow of Water at Supercritical Pressure, Heat Transfer-Sov. Res 22 (1990) 91–102.

[51] M. Bazargan, M. Mohseni, The significance of the buffer zone of boundary layer on convective heat transfer to a vertical turbulent flow of a supercritical fluid, Journal of Supercritical Fluids 51 (2009) 221–229.

[52] S. Jajja, J. Sequira, B. Fronk, Supercritical Carbon Dioxide Heat Transfer Data for Rectangular Microchannels and Micro-Pin Array with Non-Uniform Heated Boundary Condition at Reduced Pressure of 1.1, doi: 10.6084/m9.figshare.9750914.v1 (2019).

[53] J. Turner, Buoyancy Effects in Fluids, Cambridge University Press, 1973.

[54] E. Hauptmann, An experimental investigation of forced convective heat transfer to a fluid in the region of its critical point, 1966.

[55] H. Tennekes, J. Lumley, A First Course in Turbulence, The MIT Press, 1972.

[56] Q. Zhou, J. R. Taylor, C. P. Caulfield, Self-similar mixing in stratified plane Couette flow for varying Prandtl number, Journal of Fluid Mechanics 820 (2017) 86–120.

[57] A. Monin, A. Yaglom, Statistical Fluid Mechanics I, MIT Press, 1975.

[58] J. P. Hartnett, J. C. Y. Koh, S. T. McComas, A Comparison of Predicted and Measured Friction Factors for Turbulent Flow Through Rectangular Ducts, Journal of Heat Transfer 84 (1962) 82.

[59] T. M. Jeng, S. C. Tzeng, Pressure drop and heat transfer of square pin-fin arrays in in-line and staggered arrangements, International Journal of Heat and Mass Transfer 50 (2007) 2364–2375.

List of Figures

List of Tables

Nomenclature

Symbols

A	Area	m^2
C_p	Specific heat capacity	J $kg^{-1}K^{-1}$
$\bar{C_p}$	Integrated specific heat capacity	J $kg^{-1}K^{-1}$
C	Constant	–
FS	Full scale	–
D	Diameter	m
f	Friction factor	–
G	Mass flux	kg $m^{-2}s^{-1}$
g	Acceleration due to gravity	m s^{-2}
Gr_q	Grashof number based on heat flux	–
h	Specific enthalpy	J kg^{-1}
H	Height	m
ID	Internal diameter	m
K	Minor loss coefficient	–
k	Thermal conductivity	W m^{-1} K^{-1}
L	Length	m
$MAPE$	Mean absolute percent error	%

$\dot{m}$	Mass flow rate	kg s^{-1}
Nu	Nusselt number	–
P	Pressure	MPa
Pr	Prandtl number	–
$\bar{Pr}$	Integrated Prandtl number	–
$\dot{Q}$	Heat Duty	W
q''	Heat flux	W cm^{-2}
Re	Reynolds number	–
R_α	Heat transfer coefficient ratio	–
R_F	Flux Richardson number	–
S	Pin pitch	–
T	Temperature	^{o}C
x	Local position, distance	m
V	Velocity	m s^{-1}
$\triangle$	Pressure drop	Pa

Greek Letters

α	Convective heat transfer coefficient	W m^{-2} K^{-1}
β	Pitch to pin diameter ratio , $\frac{S_L}{D_h}$ or $\frac{S_T}{D_h}$	
δ	Distance	m
ϵ	Surface roughness	m

κ	Von-Karman constant	–
μ	Dynamic viscosity	kg m^{-1} s^{-1}
ν	Kinematic viscosity	m^2 s^{-1}
ρ	Density	kg m^{-3}
ψ	Acceleration parameter	
θ	Temperature scale	K
τ	Shear stress	N m^{-2}

Subscripts

acc	Acceleration	–
A, min	Minimum flow area	–
ADC	Analog-to-digital	–
$array$	Pin array	–
av	Average	–
$bulk$	Bulk fluid temperature	–
$b - IG$	Bulk evaluated ideal gas property	–
c	Cross section	–
$chan$	Channel	
$char$	Characteristic length	m
cl	conduction layer–	
cp	Connecting pipe	–

cpr	Constant property	–
$corr$	Correlation	–
D	Diagonal	–
ex	exit	–
exp	Experimental	–
$film$	Film temperature	–
fin	Fin acting as a wall between microchannels	–
$fluid$	Fluid	–
FM	Flux meter	–
$fric$	Frictional pressure drop	–
h	Hydraulic	–
i	Segment	–
in	Inlet	–
K	Kelvin	–
l	Large	–
lam	Laminar	–
MB	Miter bend	–
$minor$	Pressure drop associated with minor losses	–
$meas$	Measured	–
$normal$	Direction normal to the wall	–

out	Outlet	–
pin	Pin	–
$prec$	Precision	–
PC	Pseudo-critical	–
Q	Thermal energy	–
q	Grashof number based on heat flux	–
R	Reduced	–
s	small	–
SC	Sudden contraction	–
SE	Sudden expansion	–
sCO_2	Supercritical carbon dioxide	–
t	Thermal	–
T	Transverse	–
$theo$	Theoretical	–
th	Threshold	–
tot	Total	–
$turb$	Turbulent	–
UTC	Uncertainty total conversion	–
vpr	Variable property	–
w	Wall	–

wet	Wetted dimensions	–
Wi	Width	–